CHALMERS
UNIVERSITY OF TECHNOLOGY

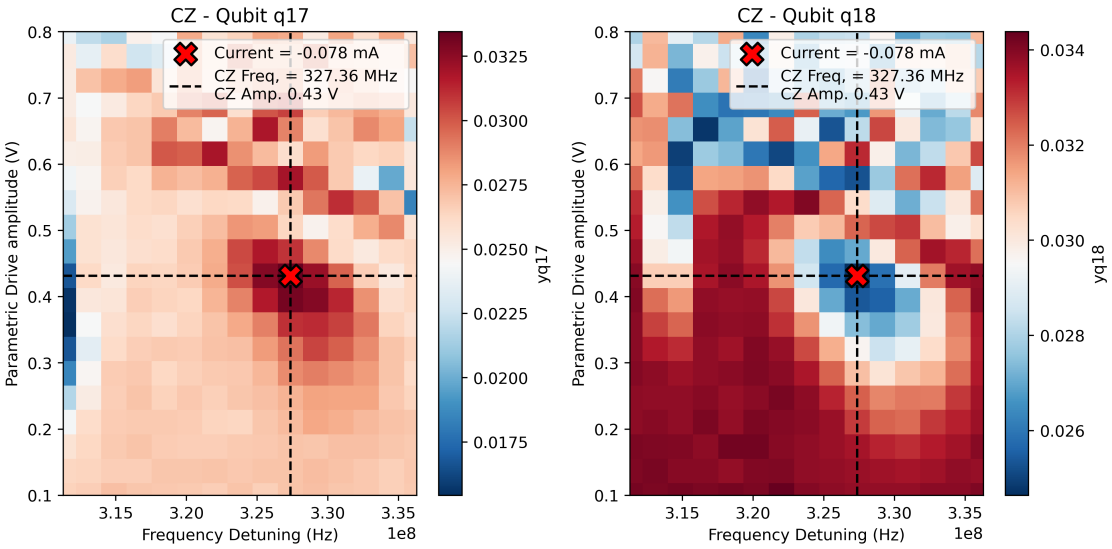


# Toward an automatic parallelized two-qubit-gate calibration

Master's thesis in Physics

Joel Sandås

DEPARTMENT OF MICROTECHNOLOGY AND NANOSCIENCE

CHALMERS UNIVERSITY OF TECHNOLOGY
Gothenburg, Sweden 2025
www.chalmers.se

Master's thesis 2025

# Toward an automatic parallelized two-qubit-gate calibration

JOEL SANDÅS


CHALMERS
UNIVERSITY OF TECHNOLOGY

Department of Microtechnology and Nanoscience
*Quantum Technologies*
Chalmers University of Technology
Gothenburg, Sweden 2025

Toward an automatic parallelized two-qubit-gate calibration
JOEL SANDÅS



Supervisor: Michele Faucci Giannelli, Department of Microtechnology and Nanoscience
Examiner: Jonas Bylander, Department of Microtechnology and Nanoscience

Master's Thesis 2025
Department of Microtechnology and Nanoscience
Qunatum Technologies
Chalmers University of Technology
SE-412 96 Gothenburg
Telephone +46 31 772 1000

Cover: Results from the CZ-parametrization

Typeset in LaTeX
Printed by Chalmers Reproservice
Gothenburg, Sweden 2025

Toward an automatic parallelized two-qubit-gate calibration
Joel Sandås
Department Of Microtechnology And Nanoscience
Chalmers University of Technology

# Abstract

Calibrating a large quantum processor is a challenging task as it requires optimizing many parameters for each gate. As the number of gates increases, the amount of human intervention must be reduced to a minimum and an automatic calibration must be developed to carry out all these complex calibrations. The quantum processor developed by the quantum computing group at Chalmers is already complex enough to require such automation, as it contains 25 qubits. The group has developed an application, called Tergite automatic calibration, that can perform single-qubit calibration but is not yet capable of calibrating two-qubit gates. This Master's thesis focuses on this crucial missing functionality; in this work, a fully automatic calibration procedure is presented that can calibrate two-qubit gates for the 25-qubit chip. Two key aspects have been considered in this work; the possibility of reliably finding operational points that can be used for the calibrations of the desired two-qubit gate and the possibility do this for multiple couplers in parallel. Robustness measurements are presented to show that the autocalibration procedure can reliably find the calibration parameters in different conditions. Crucially, the algorithm developed is not only capable of calibrating multiple two-qubit gates, but it can do so in a relatively fast enough time to allow reliable operations on the quantum processor.

Keywords: Quantum computing, Automatic Calibration, Two-qubit-gate calibrations, Parallelized Calibration, Flux-Tunable Coupler

# Acknowledgements

I would like to express my sincere gratitude to my supervisor, **Dr. Michele Faucci Giannelli**. Working with you has been easy and fun. Thank you for your continuous guidance, support, and insightful feedback throughout this thesis.
I also wish to thank Dr. Giovanna Tancredi whose valuable suggestions have greatly contributed to the final outcome of this work
Thank you to my examiner Prof. Jonas Bylander, who has guided me through the thesis.
Thank you to the other members in my group, Abdullah-Al Amin, Liangyu Chen, Theresa Fuchs and Emil Hogedal for the discussions and the collective reasoning.
My appreciation extends to the Department of Microtechnology and Nanoscience at Chalmers for providing a supportive academic environment.
Finally, I am thankful to my family and friends for their constant encouragement and support during my studies.

Joel Sandås, Gothenburg, June 2025

# Contents

# List of Figures

# List of Tables

# 1
# Introduction

Quantum computing holds the promise of solving problems that are intractable for classical computers, with potential applications in cryptography, optimization, materials science, and beyond [1, 2, 3]. However, building and operating a quantum processor that has a high number of qubits, such as those from IBM [4] and Google [5], remains one of the foremost challenges in the field. This difficulty is caused by the inherent instability of the qubits that are used to form the gates used in quantum alghoritms. To minimize the error of the gates, a quantum processor unit (QPU) need to be constantly calibrated [6, 7]. As QPUs scale up in the number of qubits, so does the complexity of the calibration. This is a significant challenge and makes the calibration as important as the fabrication process. Already with a 15-qubit processor, like in [8], a manual calibration becomes unfeasible, necessitating the development of automatic calibration procedures.

At Chalmers University of Technology, the Quantum Computing group developed a superconducting quantum processor consisting of 25 qubits [9] which is used in this work. This system is already at a scale where human-in-the-loop calibration is not only inefficient but increasingly error-prone. To address this, the group developed the `Tergite Autocalibration` application [10]. The goal of this software is to provide a fully automated calibration of the chip, however at the moment it can only facilitates the calibration of single-qubit gates since the process is still not fully automated and requires user inputs for optimizing the calibration. Furthermore, the application lacks the functionality to calibrate two-qubit gates, which are essential for performing entangling operations and executing quantum algorithms.

This Master's thesis addresses this missing capability by introducing an automatic calibration procedure for two-qubit gates, specifically targeting the Controlled-Z (CZ) gate. Two main challenges are tackled: reliably identifying working points suitable for two-qubit gate operation in an automatic way, and enabling simultaneous calibration of multiple gates. The proposed solution is integrated into the existing Tergite application, providing new capabilities to the whole research group.

Furthermore, the proposed calibration has been evaluated for its robustness and speed, demonstrating that it can find calibration parameters for all considered gates in parallel and that it can be run within a timeframe compatible with practical processor operation. The ability to calibrate multiple CZ gates in parallel and automatically represents a significant step toward a fully-functional `Tergite Autocalibration` tool.

The thesis is structured as follow; the theoretical framework of qubits and operation of CZ is described in Chapter 2. The experimental setup and the QPU are described in Chapter 3. The calibration chain, as well as several studies aimed at improving

the automation of the calibration, are described in Chapter 4. Finally, the conclusion and future direction are discussed in Chapter 5.

# 2

# Theory

Since the thesis focusses on the calibration procedure for superconducting-based quantum processors, this Chapter will lay down the basic theoretical background on superconducting circuits and quantum operations.

## 2.1 Qubit gates and Block sphere representation

In quantum computation, the fundamental unit of information is the *qubit*, which differs from a classical bit by being capable of existing in a superposition of its basis states. A qubit's state can be written as [11]:

$$|\psi\rangle = \alpha\,|0\rangle + \beta\,|1\rangle\,, \quad \text{with} \quad |\alpha|^2 + |\beta|^2 = 1, \tag{2.1}$$

where $\alpha, \beta \in \mathbb{C}$ and $|0\rangle\,, |1\rangle$ are the computational basis states.

### 2.1.1 Bloch Sphere Representation

The Bloch sphere offers a geometric perspective of a single qubit's pure state. By excluding the global phase, any state of a single qubit can be expressed as:

$$|\psi\rangle = \cos\left(\frac{\theta}{2}\right)|0\rangle + e^{i\phi}\sin\left(\frac{\theta}{2}\right)|1\rangle\,, \tag{2.2}$$

where $\theta \in [0, \pi]$ and $\phi \in [0, 2\pi]$ are the spherical coordinates [11]. This formulation maps the qubit's state to a point on the unit sphere's surface in $\mathbb{R}^3$, called the Bloch sphere, see figure 2.1. The coordinates $(x, y, z)$ of the Bloch vector associated with $|\psi\rangle$ are:

$$x = \sin\theta\cos\phi, \quad y = \sin\theta\sin\phi, \quad z = \cos\theta. \tag{2.3}$$

This representation is particularly useful for visualizing single-qubit gates as rotations on the Bloch sphere.

### 2.1.2 Single-Qubit Quantum Gates

Quantum gates are unitary operations that evolve the state of a qubit. For a single qubit, gates are represented by $2 \times 2$ unitary matrices. Common single-qubit gates include:

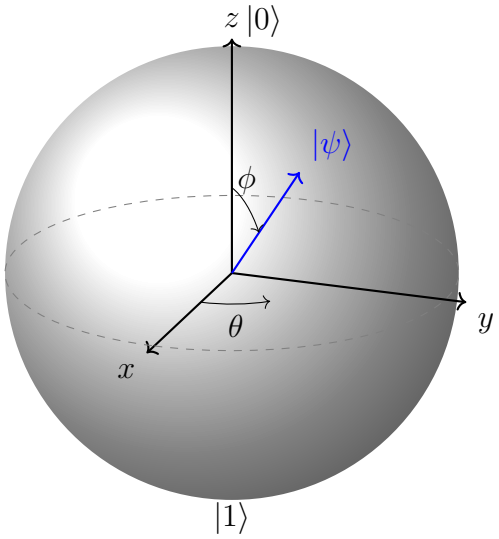


**Figure 2.1:** Illustrates a Bloch sphere. A state $|\psi\rangle$ can be described as a point on the Bloch sphere. Applying gates will move this point around the Bloch sphere.

- **Pauli Gates**:

$$X = \begin{pmatrix} 0 & 1 \\ 1 & 0 \end{pmatrix}, \quad Y = \begin{pmatrix} 0 & -i \\ i & 0 \end{pmatrix}, \quad Z = \begin{pmatrix} 1 & 0 \\ 0 & -1 \end{pmatrix}.$$

  These correspond to 180-degree rotations around the $x$, $y$, and $z$ axes of the Bloch sphere, respectively.
- **Hadamard Gate (H)**:

$$H = \frac{1}{\sqrt{2}} \begin{pmatrix} 1 & 1 \\ 1 & -1 \end{pmatrix}. \tag{2.4}$$

  The Hadamard gate maps basis states to equal superpositions, effecting a rotation that brings the state vector onto the $x$–$z$ plane of the Bloch sphere.
- **Phase Gates**:

$$S = \begin{pmatrix} 1 & 0 \\ 0 & i \end{pmatrix}, \quad T = \begin{pmatrix} 1 & 0 \\ 0 & e^{i\pi/4} \end{pmatrix}.$$

  These gates apply phase shifts, corresponding to rotations about the $z$-axis.
- **Rotation Gates**:

$$R_x(\theta) = e^{-i\theta X/2} = \cos\left(\frac{\theta}{2}\right) I - i \sin\left(\frac{\theta}{2}\right) X,$$
$$R_y(\theta) = e^{-i\theta Y/2}, \quad R_z(\theta) = e^{-i\theta Z/2}.$$

  These provide continuous rotations around the respective axes and are central in constructing arbitrary single-qubit operations.

### 2.1.3 Two-Qubit System

A qubit is represented by a two-level quantum system, with the computational basis states denoted as $|0\rangle$ and $|1\rangle$. For a system of two qubits, the combined Hilbert space

is the tensor product of the individual qubit spaces, resulting in a four-dimensional state space:

$$\mathcal{H} = \mathcal{H}_1 \otimes \mathcal{H}_2. \tag{2.5}$$

The computational basis for the two-qubit system is given by [11]:

$$\{|00\rangle, |01\rangle, |10\rangle, |11\rangle\}, \tag{2.6}$$

where, for example, $|10\rangle = |1\rangle \otimes |0\rangle$ denotes the first qubit in state $|1\rangle$ and the second in state $|0\rangle$.
The general pure state of a two-qubit system can be written as a linear combination of the basis states:

$$|\psi\rangle = c_{00}|00\rangle + c_{01}|01\rangle + c_{10}|10\rangle + c_{11}|11\rangle, \tag{2.7}$$

where $c_{ij} \in \mathbb{C}$ and normalization requires

$$|c_{00}|^2 + |c_{01}|^2 + |c_{10}|^2 + |c_{11}|^2 = 1. \tag{2.8}$$

Operators acting on two-qubit systems are formed using tensor products of single-qubit operators. For example, if $X$ and $I$ denote the Pauli-X and identity operators, respectively, then the operator $X \otimes I$ flips the first qubit and leaves the second unchanged. A generic two-qubit operator can be expressed as a $4 \times 4$ matrix.
In this thesis, the notion of control and target qubit is used. Meaning, for example, that qubit 1 acts as the control qubit and qubit 2 as the target qubit.

### 2.1.4 CZ Gate and Phase Accumulation

Two-qubit entangling gates are a cornerstone of universal quantum computation. The Controlled-Z (CZ) gate is a diagonal two-qubit gate that applies a $\pi$ phase shift to the $|11\rangle$ state, leaving all other computational states unchanged. In ideal form, it is represented by the matrix, [11]:

$$U_{\mathrm{CZ}} = \begin{pmatrix} 1 & 0 & 0 & 0 \\ 0 & 1 & 0 & 0 \\ 0 & 0 & 1 & 0 \\ 0 & 0 & 0 & -1 \end{pmatrix}. \tag{2.9}$$

In physical systems, however, the implementation of the CZ gate is accompanied by various dynamical and geometric phases. These phases arise from interactions with higher excited states (e.g., $|20\rangle$ or $|02\rangle$), residual couplings, and pulse imperfections. As a result, the actual gate unitary takes a more general diagonal form, as seen in the matrix below [12]:

$$U_{\mathrm{CZ}_{\phi_g}} = \begin{pmatrix} 1 & 0 & 0 & 0 \\ 0 & e^{-i\phi_{01}} & 0 & 0 \\ 0 & 0 & e^{-i\phi_{10}} & 0 \\ 0 & 0 & 0 & e^{-i(\phi_g+\phi_\zeta+\phi_{10}+\phi_{01})} \end{pmatrix}. \tag{2.10}$$

This matrix representation reflects the physical evolution of a two-qubit system during a CZ gate and is expressed in the computational basis $\{|00\rangle, |01\rangle, |10\rangle, |11\rangle\}$.

The phases $\phi_{01}$ and $\phi_{10}$ correspond to dynamical phases accumulated by the second and first qubit, respectively, when the other qubit is in its ground state. These arise from slight detunings or interactions with control pulses during the gate duration. They are effectively single-qubit $Z$ rotations and can be corrected using virtual Z-gates (frame updates) or calibrated out in post-processing.

The term $\phi_g$ represents the desired entangling phase of the CZ gate. For a perfect CZ gate, this phase should be $\pi$, implementing the $-1$ on the $|11\rangle$ state. In practice, $\phi_g$ can deviate from this value due to over/under rotation of the gate pulse or calibration errors.

The term $\phi_\zeta$ in the unitary matrix represents a geometric phase that can, in principle, accumulate when a quantum system undergoes cyclic or adiabatic evolution in Hilbert space. In some physical implementations of the CZ gate, particularly those involving slow adiabatic flux pulses, this phase emerges from the curvature of the parameter space through which the quantum state evolves. However, in most practical implementations of the CZ gate in fixed-frequency or near-adiabatic regimes, the system dynamics are engineered such that any geometric contribution to the overall phase is effectively cancelled or rendered negligible. As a result, it is common and well-justified to assume $\phi_\zeta = 0$ when analysing and calibrating the CZ gate.

The lower-right element of the matrix includes all the accumulated phases:

$$\phi_{11} = \phi_g + \phi_\zeta + \phi_{10} + \phi_{01}. \tag{2.11}$$

This total phase determines the action of the gate on the $|11\rangle$ state. To extract a clean CZ gate, one must remove or compensate for all extraneous phases except the entangling phase $\phi_g$. This is typically done via calibration sequences or virtual Z-gates applied before or after the CZ gate, transforming the raw unitary into its canonical form.

Since the CZ gate introduces known phase shifts to each computational state, these can be reversed using virtual Z-gates (which are implemented in software by rotating the phase of future pulses). The corrected form of the gate then becomes [13]

$$U_{\text{CZ corrected}} = (Z_1 Z_2)\, U_{\text{CZ}_{\phi_g}} \tag{2.12}$$

where $Z_1$ and $Z_2$ are single-qubit Z rotations applied to qubits 1 and 2. This procedure restores the gate to its ideal CZ form.

The CZ-gate also plays a foundational role in constructing more complex two-qubit gates, such as the CNOT and SWAP gates. By combining the CZ gate with single-qubit Hadamard gates, one can implement a CNOT gate using the identity $\text{CNOT} = (I \otimes H)\,\text{CZ}\,(I \otimes H)$, where $H$ is the Hadamard gate and $I$ is the identity. The CZ gate introduces a conditional phase flip when both qubits are in the $|1\rangle$ state, which, through basis transformation, results in conditional bit flips. Similarly, a SWAP gate can be decomposed into three CNOT gates: $\text{SWAP} = \text{CNOT}_{12}\,\text{CNOT}_{21}\,\text{CNOT}_{12}$, and each CNOT in this sequence can be built from a combination of CZ and Hadamard gates. Thus, the CZ gate serves as a universal entangling primitive in many two-qubit gate constructions.

## 2.2 Superconducting qubits

### 2.2.1 Josephson junction

A Josephson junction (JJ) consists of a thin insulating layer positioned between two superconducting layers. Named after Brian Josephson, these devices are based on his 1962 prediction that superconducting electron pairs can "tunnel" across the nonsuperconducting barrier linking the two superconductors [14].
When many metals and alloys are cooled to temperatures near absolute zero (usually within 20 degrees or less), they undergo a phase transition. At this "critical temperature," the material shifts from its normal state, marked by electrical resistance, to a superconducting state where direct electrical current encounters virtually no resistance.
This phenomenon arises as the electrons within the metal form pairs. Above the critical temperature, the interaction between two electrons tends to be repulsive. However, once below this threshold, the interaction becomes faintly attractive, influenced by the electrons' interactions with the metal's ionic lattice.
This slight attraction enables them to reach a lower energy state, which creates an energy "gap." Due to this gap and the reduced energy state, electrons can traverse the material without being deflected by the lattice ions, allowing current to flow freely. When electrons are scattered by ions, this leads to electrical resistance in metals. In a superconductor, however, there is no electrical resistance, ensuring that no energy is lost.
Mathematically, the Josephson junction is described by the following two fundamental relations [15]:

$$I = I_c \sin \phi, \tag{2.13}$$

$$V = \frac{\hbar}{2e} \frac{d\phi}{dt}, \tag{2.14}$$

where $I$ is the supercurrent through the junction, $I_c$ is the critical current, $\phi$ is the superconducting phase difference across the junction, and $V$ is the voltage across it. These expressions reveal the non-linear relationship between current and phase, distinguishing the Josephson junction from a traditional linear inductor.

### 2.2.2 Transmon, a superconducting qubit

One of the most promising implementations of a qubit is the superconducting qubit [16]. Among the different types of superconducting qubits, the *transmon qubit* stands out due to its relative simplicity and robustness against charge noise [17, 18]. The transmon qubit consists of a Josephson Junction in parallel with a shunt capacitor, see circuit diagram in Fig. 2.2. The Josephson junction introduces a crucial nonlinearity into the system, acting as a non-linear inductor whose inductance depends on the phase difference across the junction. When this non-linear inductor is combined with a shunt capacitor, the resulting circuit behaves as an anharmonic oscillator.

The quantum mechanical treatment of this system leads to the following Hamiltonian for the transmon [19]:

$$\hat{H} = 4E_C(\hat{n} - n_g)^2 - E_J \cos\hat{\phi}, \tag{2.15}$$

where $E_C$ is the charging energy associated with the shunt capacitance $C$, $E_J$ is the Josephson energy, $\hat{n}$ is the number operator representing the number of excess Cooper pairs on the island, $\hat{\phi}$ is the phase difference operator across the junction, and $n_g$ is the offset charge controlled by a gate voltage.
The transmon operates in a regime where the Josephson energy $E_J = \frac{\phi_0 I_c}{2\pi}$ dominates over the charging energy $E_C = \frac{e^2}{2C}$. This significantly reduces sensitivity to charge fluctuations, which are a major source of decoherence in superconducting circuits [17]. As a result, transmons exhibit improved coherence times while maintaining sufficient anharmonicity for reliable qubit control and readout [20]. The anharmonicity ensures separation between the computational states. The transmon can therefore be controlled between the computational states without inadvertently exciting higher energy levels. Its compatibility with microwave circuitry also makes it well-suited for integration into scalable quantum computing architectures.

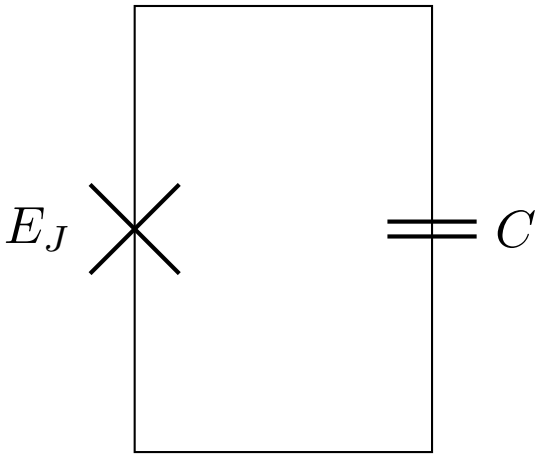


**Figure 2.2:** Schematic circuit diagram of a transmon qubit. The transmon consists of a Josephson junction (represented here as a cross) shunted by a large capacitance $C$, forming a weakly anharmonic oscillator. The Josephson energy $E_J$ and charging energy $E_C$ define the qubit's energy levels.

In the transmon regime, the ratio $E_J/E_C \gg 1$, typically on the order of 50 to 100, which leads to a potential energy landscape resembling a cosine function that is nearly harmonic close to its minimum, but with sufficient anharmonicity to allow distinguishing and manipulating specific of quantum transitions [17]. The eigenstates of the Hamiltonian represent quantised energy levels within this potential well. Because of the cosine term, the level spacing is not uniform. This allows the isolation of the lowest two energy levels, which can be interpreted as the qubit states $|0\rangle$ and $|1\rangle$. The approximate energy of the $m$-th level can be expressed as [21]:

$$E_m \approx -E_J + \sqrt{8E_J E_C}\left(m + \frac{1}{2}\right) - \frac{E_C}{4}(2m^2 + 2m + 1) \tag{2.16}$$

where $\omega_{01} \approx \sqrt{8E_J E_C}$ is the transition frequency between the ground state $|0\rangle$ and the first excited state $|1\rangle$, and the term proportional to $E_C$ introduces an anharmonic correction. For a harmonic oscillator, this correction would be zero, and all transitions would be equally spaced, making it impossible to isolate a two-level system (see the left plot in Fig. 2.3. However, in the transmon, the transition frequency between $|1\rangle$ and $|2\rangle$ is reduced by the anharmonicity:

$$\omega_{12} = \omega_{01} - \alpha, \tag{2.17}$$

with $\alpha \approx E_C$ being the anharmonicity of the system. This separation ensures that when a microwave drive is applied at the frequency $\omega_{01}$, it predominantly excites the $|0\rangle \leftrightarrow |1\rangle$ transition, leaving higher states effectively unpopulated during standard qubit operations, as the right figure in 2.3.

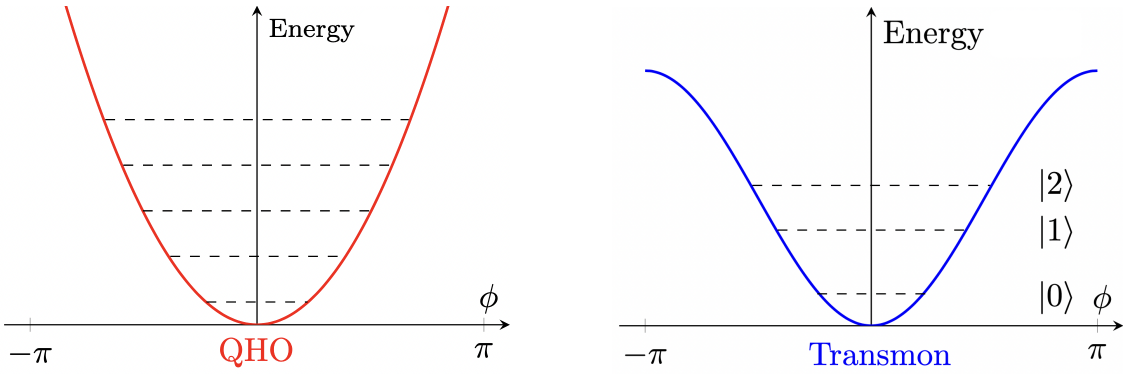


**Figure 2.3:** Comparison of the potential and energy level spacing of a quantum harmonic oscillator (QHO, left) and a transmon qubit (right). The QHO features equally spaced energy levels, making it unsuitable for qubit implementation due to the non-addressability of transitions. In contrast, the transmon potential exhibits anharmonicity, leading to unequally spaced levels that enable selective control of the $|0\rangle \rightarrow |1\rangle$ transition.

The anharmonicity, while small compared to the absolute energy levels (typically on the order of hundreds of MHz, compared to transition frequencies in the GHz range), plays an essential role in enabling high-fidelity qubit control [22]. It allows qubit gates to be performed without leakage into higher energy levels, thereby justifying the truncation of the Hilbert space to a two-level system. This truncation is the foundation of qubit logic, where operations are defined solely within the subspace spanned by $\{|0\rangle, |1\rangle\}$.
In conclusion, one can think of the transmon as essentially an artificial atom constructed from superconducting materials, operating at cryogenic temperatures where resistive losses are negligible [23].

### 2.2.3 Flux-Tunable Transmons

Given a certain $E_C$ and $E_J$, the frequency $\omega_{01}$ of the transmon qubit is fixed. However, if one uses two Josephson Junctions in parallel (aka. a SQUID), the Josephson energy becomes now dependent on the magnetic flux $\Phi$ threading the SQUID loop.

This allows us to control the frequency of the transmon by applying an on-chip current that generates the magnetic flux through the SQUID. In the context of this thesis, flux-tunable transmons are referred to as couplers as they are used to mediate the interactions between fixed-frequency transmon qubits to which they are coupled to. The couplers are flux-biased to modify their effective interaction with the neighbouring qubits, making tunable exchange-type interactions possible [24].
By varying the magnetic flux through the coupler loop, the coupler frequency $\omega_C$ can vary, effectively controlling the energy detuning between the coupler and the qubits. If a coupler is coupled to two qubits ($Q_1$, $Q_2$), this adjusts the effective coupling strength between $Q_1$ and $Q_2$. When the coupler is detuned far from both qubits, the effective interaction is minimized; when it is brought near resonance, the interaction is enhanced.

## 2.3 Parametric Two-Qubit Gates

To achieve high-fidelity two-qubit gates, parametric control has become a go-to method for superconducting qubits. The advantages of the parametric gates are the time-dependent changes in system parameters to trigger or enhance certain interaction terms in the system's Hamiltonian. With this technique, dynamic control over entangling interactions is possible, often without needing direct adjustments to the qubit-qubit coupling.
A parametric two-qubit gate is the *parametric CZ gate*, which works through flux modulation in superconducting qubits. This was first demonstrated in [25]. By modulating one qubit's transition frequency periodically, a resonance condition is created between the computational states and a non-computational state, which enables a conditional phase to be created [13]. The effective interaction is facilitated by higher energy levels and can be expressed using a time-dependent Hamiltonian in the rotating frame[26]:

$$H_{\text{int}}(t) = \sum_{i,j} g_{ij}(t)\sigma_i^{\alpha}\sigma_j^{\beta}, \tag{2.18}$$

where $g_{ij}(t)$ represents the time-dependent coupling terms shaped by modulation, and $\sigma_i^{\alpha}$ indicates the Pauli operators acting on qubit $i$.
With parametric driving, it is possible to selectively activate interactions based on frequency-matching conditions. This results in gate operations that are both switchable and tunable. The parametric gates are compatible with fixed-frequency qubits, which generally exhibit better coherence properties. Parametric schemes can also help reduce unwanted crosstalk, enhancing scalability in multi-qubit systems.

# 3
# Chip design

## 3.1 Quantum Processor Architecture

This section describes the architecture of the quantum processor used in this work, additional information can be found in [9]. The processor is built using a two-tier flip-chip design that separates quantum components (qubits and couplers) from control and readout circuitry. This modular approach improves signal routing, fabrication efficiency, and scalability.

### 3.1.1 Flip-Chip Stack and Materials

The quantum processor comprises two vertically integrated chips: a quantum chip (Q-chip) and a classical control chip (C-chip). The Q-chip, fabricated on a silicon substrate, hosts the superconducting transmon qubits and tunable couplers. The C-chip, positioned beneath the Q-chip and also fabricated on silicon, contains the control wiring, microwave drive lines, and readout resonators. See circuit diagram in Fig 3.1.
These two chips are bonded face-to-face using superconducting indium bump bonds, which establish both mechanical support and electrical grounding. The target spacing between the chips is approximately 8 µm [9], shown in Fig. 3.2. The material stack is engineered to optimize performance, for example, the Q-chip and C-chip feature aluminum structures for qubits, coupler and resonator and utilize niobium nitride (NbN), underbump layer for the low-loss interconnecting indium bonds.

### 3.1.2 Qubit Layout and Signal Routing

The processor features a two-dimensional grid of 25 qubits arranged in a $5 \times 5$ square lattice, with a center-to-center pitch of 2 mm. Each qubit is connected to its nearest neighbors via tunable couplers, enabling two-qubit gate operations across the lattice. The physical layout is designed to ensure that signal lines for qubit control and readout do not cross each other, which is achieved by careful vertical stacking and routing across both chips.
The C-chip contains three key signal lines for each qubit:

- An **xy line**, used to deliver microwave pulses for single-qubit gate operations.
- A **z line**, implemented as a superconducting loop to provide flux biasing to the SQUID in each coupler, enabling frequency tuning.
- A **readout resonator**, typically a $\lambda/4$ coplanar waveguide resonator, used for dispersive qubit readout with 5 resonators coupled to the same feedline for

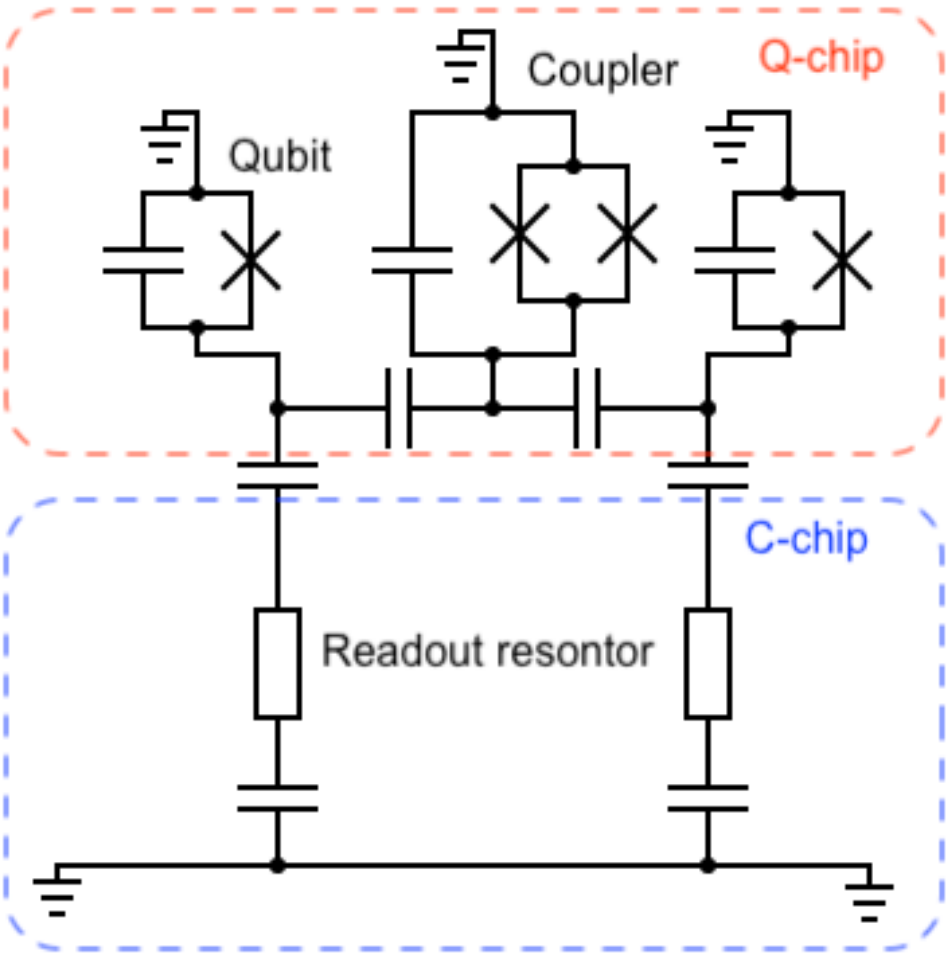


**Figure 3.1:** The circuit diagram of the two-qubit pair design with the Q-chip and C-chip separated

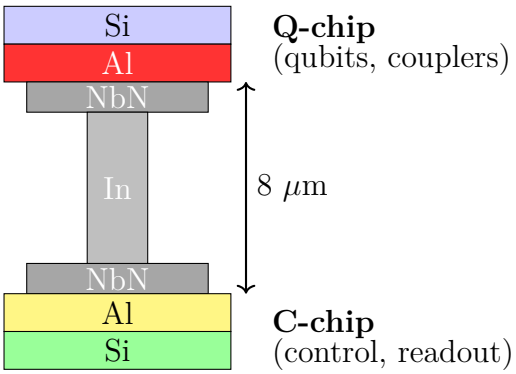


**Figure 3.2:** Cross-sectional schematic of a flip-chip integrated quantum processor. The Q-chip (top) contains the qubits and couplers, while the C-chip (bottom) contains the control and readout circuitry. The chips are connected via an indium bump and separated by an 8 $\mu$m gap.

simultaneous readout of 5 qubits.
Each of these lines is positioned directly beneath its corresponding component on the Q-chip to minimize crosstalk and maximize coupling efficiency.

### 3.1.3 Qubit-Coupler-Qubit (QCQ) Architectures

The 25-qubit processor is based on an architecture in which fixed-frequency qubits are pairwise coupled capacitatively to a tunable coupler,as shown in Fig. 3.5. The direct capacitive or inductive coupling between qubits is minimized, and instead, interaction is mediated via the flux-tunable coupler. This configuration provides dynamic control over the effective qubit-qubit coupling strength, allowing high-fidelity gate operations and suppression of unwanted crosstalk.

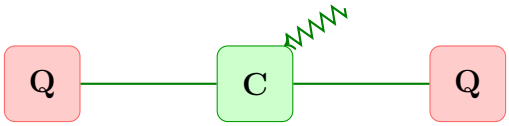


**Figure 3.5:** Schematic of the QCQ architecture.

## 3.2 Qubit Indexing and Frequency Assignment

Each qubit in the grid is assigned a unique index from 1 to 25 in a row-major format, beginning in the top-left corner and proceeding left to right and top to bottom, illustrated in Fig. 3.3. To facilitate scalable control and reduce frequency collisions, the qubits are grouped into eight frequency subgroups [27].
In the eight-frequency subgroup, the transmons are divided into two classes with different anharmonicities. These are labelled as $a_k$ (lower frequency) and $b_k$ (higher frequency), with $k = 1,2,3,4$ indicating subgroup variants. These subgroups are tiled across the chip in a repeating unit-cell pattern that ensures neighbouring qubits belong to different frequency classes, shown in Fig. 3.4. This scheme is optimized

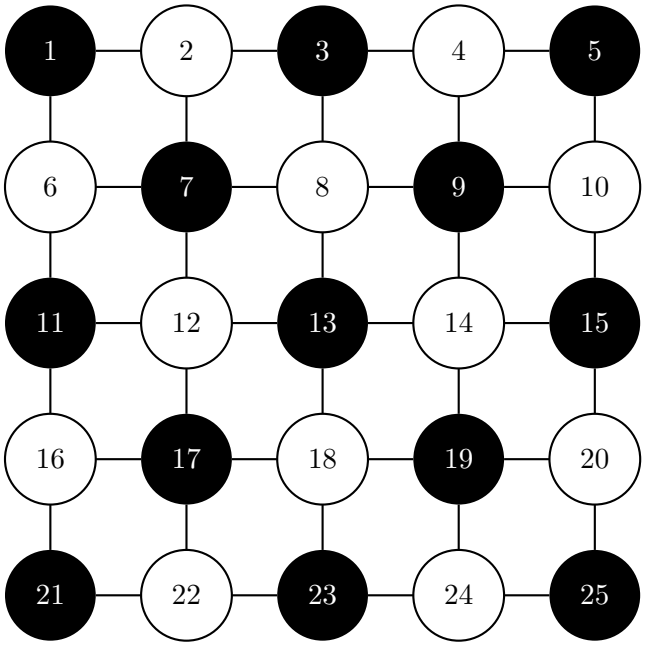


**Figure 3.3:** Schematic of the 25-qubit chip with the qubit numbers. In this thesis, qubits 16-20 are primarily used.

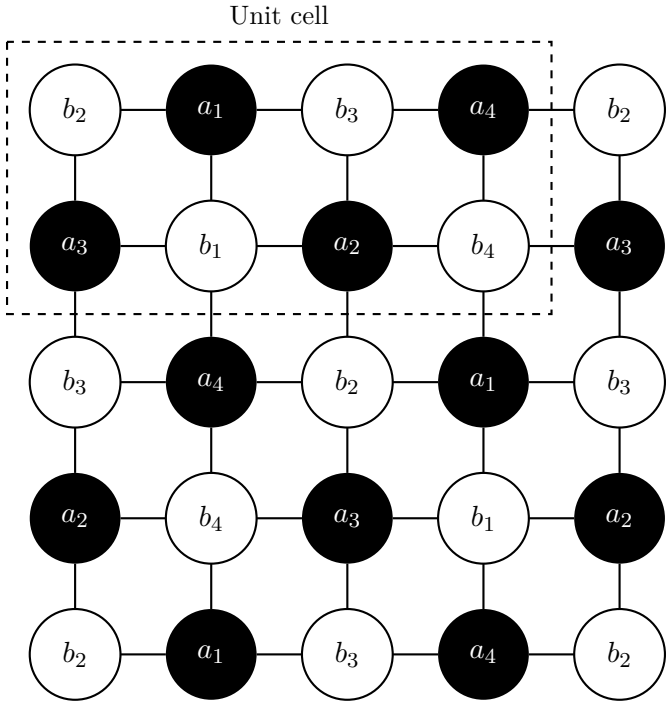


**Figure 3.4:** Schematic of the frequency allocation: The filled and empty circles represent transmons with two distinct anharmonicities; $a_k$ and $b_k$ denote different qubit frequencies, where $a_k < b_k$, resulting in a combination of eight unique frequencies arranged as shown in the diagram.

for the CZ-gate operation. Having high (control qubits) and low (target qubits) frequencies makes it easier to implement a CZ-gate. This forces the qubit to take either role, independent of which coupler it belongs to.

## 3.3 Design Considerations for Scalable Systems

This architecture reflects key principles for building scalable quantum systems:

- **Modularity:** Independent optimization of Q-chip and C-chip enables parallel development and easier debugging.
- **Signal integrity:** Physical isolation and orthogonal routing reduce decoherence and crosstalk.
- **Frequency planning:** Tiling qubits with a systematic frequency scheme supports error correction and parallel operation.

Together, these design elements form a robust foundation for medium-scale quantum processors and can be extended to larger systems with minimal architectural changes.

To be able to calibrate the entire chip, the calibration procedure needs to be performed four times. This is because each coupler is coupled to two qubits. To calibrate a CZ gate, by controlling the magnetic flux through a coupler, both of the coupled qubits are needed, meaning that the same qubits can not be used to calibrate another coupler at the same time. This results in the need to repeat the calibration procedure four times to calibrate all two-qubit gates in the device.

## 3.4 Setup used in this work

In the experiments, Qblox´s clusters [28] are used to operate the quantum processor by sending and receiving microwave pulses to/from the quantum processor, which is located inside a Bluefors dilution refrigerator. The clusters enable microwave pulses to be sent to the processor with specific amplitudes, durations and frequencies. They also receive the readout microwave pulses transmitted from the processor, convert to the hundreds of MHz range to be recorded and integrated.

Additionaly, Qblox´s SPI-racks [29] were also used. The SPI-rack generates DC current that is sent to the coupler to provide a stable magnetic flux. A picture of the lab is presented in Fig. 3.6 so that the reader can get an understanding on how the setup looks like.

Quantify [30] is used to communicate between the `Terigite Autocalibration` and the experimental apparatus (clusters and SPI-racks). Quantify is a Python-based data acquisition framework that allows communication from the codebase to the clusters (SPI-racks) for applying the desired microwave pulses (DC current).

**Figure 3.6:** This picture shows the setup in the lab. On the right, the white cylinder is the dilution fridge. Below (in the picture), the SPI-rack is located. The QBlox clusters are the blue boxes in the top part of the racks on the left of the picture.

# 4

# Calibration sequence

The calibration steps are executed in `Terigite Autocalibration` [10]. This is a Python based application that is part of the Tergite software stack designed to operate the Chalmers QPUs. Hence, this application not only performs the calibration but also needs to allow monitoring of the performance, via plots, and store them in a database so that the calibration can be used to run algorithms. The ensuing results are derived from `Terigite Autocalibration`, which allows measurements and plot generation. The `Terigite Autocalibration` software provides experiments packaged as nodes that enable calibrations to be run in a chain. The whole chain is illustrated in Fig. 4.1 and the extracted parameter of each node type is presented in Table 4.1. Each node consists of a measurement followed by an analysis. The measurements are written in Quantify, the software that allows operating the QBlox instruments.

From this the subchapters will have the same names as nodes as they are presented in the Figure 4.1.

| **Calibration** | **Parameter/information extracted** |
|---|---|
| Resonator spectroscopy | Resonator frequency |
| Qubit spectroscopy | Qubit frequency and pulse amplitude |
| Rabi oscillations | Optimal $\pi$-pulse amplitude |
| Ramsey correction | Qubit frequency correction |
| Motzoi calibration | Motzoi parameter |
| n-Rabi calibration | $\pi$-pulse amplitude correction with Motzoi parameter |
| Qubit spectroscopy with flux sweep | Coupler frequency as a function of flux |
| Resonator spectroscopy with flux sweep | Coupler frequency as a function of flux |
| CZ current from spectroscopies | Flux working point candidates |
| CZ parametrization with fixed duration | Amplitude and frequency for CZ-gate |
| CZ calibration | Selection of the best possible working point |
| CZ dynamic phase | Local phase shifts for the CZ-gate |

**Table 4.1:** This table summarizes all the calibration steps and what parameters or information are extracted from the different calibration steps.

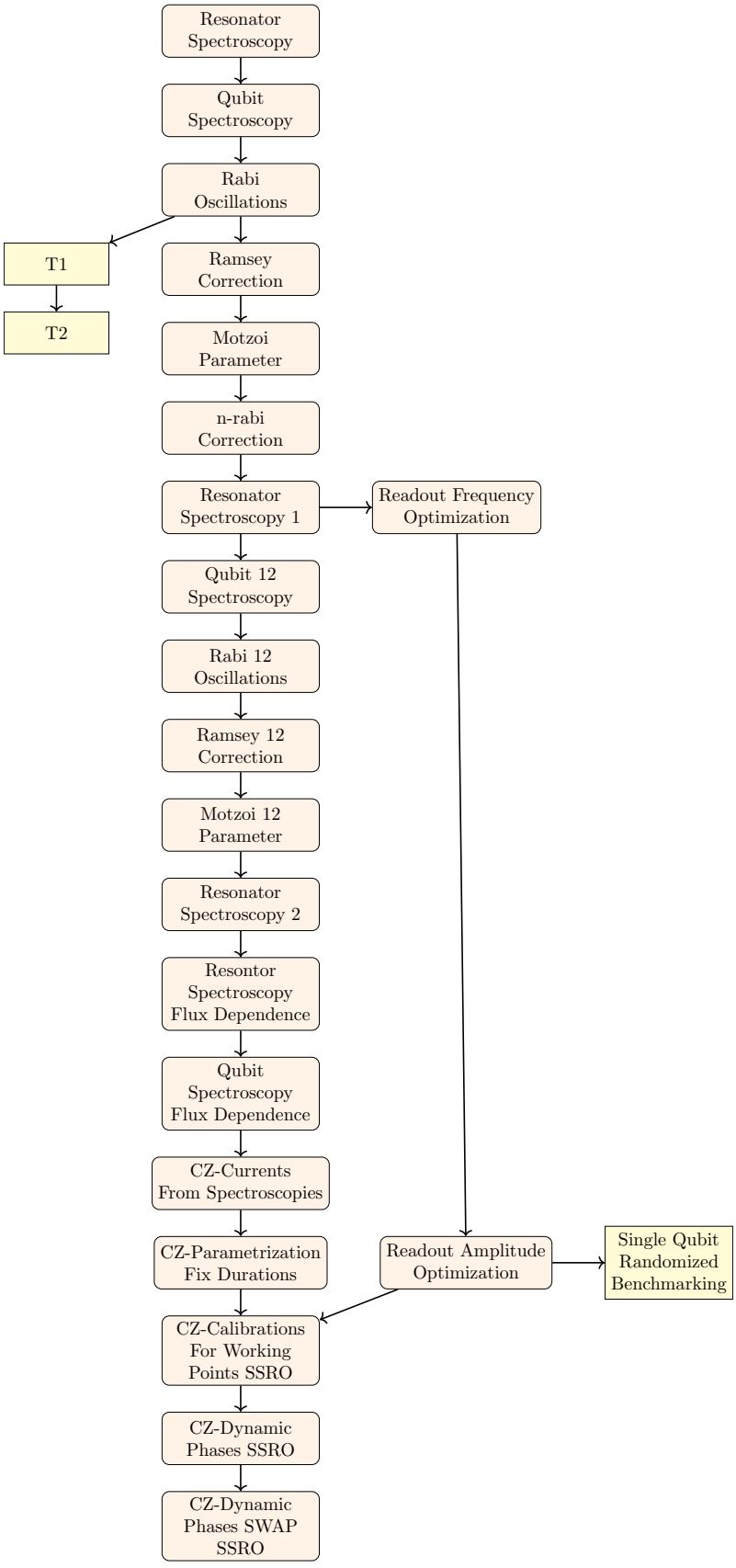


**Figure 4.1:** The schedule shows all the calibration steps in order.

While the ambition of `Terigite Autocalibration` is to be a fully automated application providing a good calibration without human intervention, currently the software does not provide such optimization and need to be run mutliple times by an user to achieve optimal performance by adjusting many parameters such as RO amplitudes, attenuations and many analysis parameters that are specific to the operated QPU. Several of the studies presented in this chapter provide crucial information to further develop the application toward full automation.

## 4.1 Single-Qubit Calibration Techniques

Single-qubit calibration refers to a sequence of experimental procedures that enable accurate state preparation, coherent manipulation, and measurement of a qubit. In this section, a theoretical explanation of the core calibration techniques in a transmon-based superconducting qubit platform and the corresponding results are presented. The calibrations are done simultaneously on qubits 17-20.

### 4.1.1 Resonator Spectroscopy

In a circuit quantum electrodynamics (cQED) architecture, each qubit is dispersively coupled to a readout resonator [31]. The resonator acts as a probe for the qubit state, and its resonance frequency shifts slightly depending on whether the qubit is in $|0\rangle$, $|1\rangle$ or $|2\rangle$. This state-dependent frequency shift allows indirect qubit readout by monitoring the transmission or reflection of microwave signals through the resonator. Resonator spectroscopy involves sweeping a probe tone across a range of frequencies near the resonator's expected resonance. The presence of a dip in the scattering parameter $S_{21}$ indicates the resonator's frequency, which can then be associated with a specific qubit state. This measurement provides initial estimates for the readout frequency.

In the dispersive regime, the resonator acts as a Lorentzian notch filter. As the probe frequency approaches the resonator's resonance frequency, the transmission dips, producing a characteristic Lorentzian-shaped dip in the amplitude [32]. The minimum of this dip corresponds to the resonator frequency for a particular qubit state.

To extract the resonance frequency, the measured transmission data is fitted to a Lorentzian model:

$$T(f) = A\left[1 - \frac{B}{1 + 4\left(\frac{f-f_r}{\kappa}\right)^2}\right],$$

where $f_r$ is the resonator frequency, $\kappa$ is the linewidth, and $A$, $B$ are fitting parameters accounting for signal offset and dip depth. This fit allows precise estimation of $f_r$ for a given qubit state.

The results from resonator spectroscopy clearly show a significant drop in transmission, which is expected given that resonator spectroscopy rarely produces errors. The measurement takes 50 measurements from different frequencies in a 3 MHz range. The results from the resonator spectroscopy can be seen in Figure 4.2. It

is important that the centre point of the frequency sweep should be the resonator frequency. If the resonator frequency is ill-centred, it can lead to problems in the coming measurements.

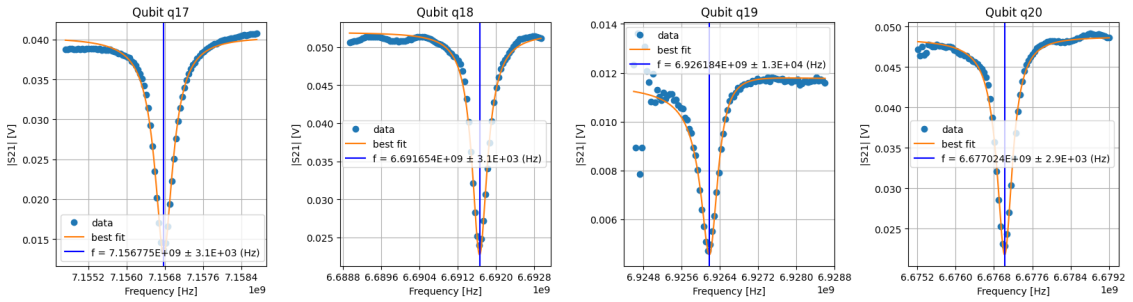


**Figure 4.2:** Results from resonator spectroscopy. The dip in the transmission is where the resonator has its resonance frequency.

### 4.1.2 Qubit Spectroscopy

The qubit spectroscopy is performed to measure the transition frequency between ground and first excited state $\omega_{01}$. This measurement is performed using a continuous wave drive tone to the qubit, illustrated in Figure 4.3. The amplitude of the drive pulse is also swept to find the optimal driving amplitude. When the drive frequency matches the $|0\rangle \leftrightarrow |1\rangle$ or $|1\rangle \leftrightarrow |2\rangle$ transition, the qubit population changes, leading to a measurable shift in the resonator's response [33]. A typical spectroscopy scan reveals a resonance peak at the transition frequency.
The $0 \rightarrow 1$ spectroscopy measurement is implemented by initializing each qubit to the ground state by letting the qubits relax, then applying a spectroscopy pulse with a frequency that is varied. After the pulse, the qubit state is measured via the resonator, and the qubit is reset by relaxing the qubit to prepare for the next iteration. When measuring the $1 \rightarrow 2$ frequency, an $X$ gate is applied before the spectroscopy pulse to transfer population to $|1\rangle$.


**Figure 4.3:** Pulse sequence for qubit spectroscopy. The qubit is first initialized to the ground state $|0\rangle$ by relaxing the qubit. A spectroscopy pulse with variable frequency $f$ is applied to drive the qubit transition $|0\rangle \rightarrow |1\rangle$. Finally, the qubit state is measured by probing the readout resonator. This sequence is repeated over a range of frequencies to identify the qubit transition frequency by detecting the resonance condition where the spectroscopy pulse excites the qubit.

The frequency sweep is combined with optional amplitude sweeps to find the optimal drive power that excites the qubit effectively without causing power broadening or unwanted transitions.
The resulting data is analyzed by using peak-finding algorithms on the measured 2D distribution of transmission amplitude versus drive frequency to locate the bin

with the highest magnitude to select both the qubit transition frequency $\omega_{01}$ and pulse amplitude. These calibrated parameters are then used to set the qubit drive frequency and power for subsequent gate calibrations.
The frequency is scanned through 51 points within a 30 MHz range, alongside an amplitude sweep involving 5 points between 1 mV and 8 mV. The peak value from these is utilized for both qubit spectroscopy and qubit amplitude, see Figure 4.4. Achieving reliable results can be challenging, particularly when processes are conducted simultaneously. Accurate results are contingent upon proper attenuation and measurement pulse amplitude settings. These values must be precisely adjusted to ensure high-quality qubit spectroscopy. A potential issue is that the measurement pulse amplitude of other qubits can interfere with the qubit of interest. Currently, there is no automated solution; the only recourse is to manually seek optimal values for accurate measurements.

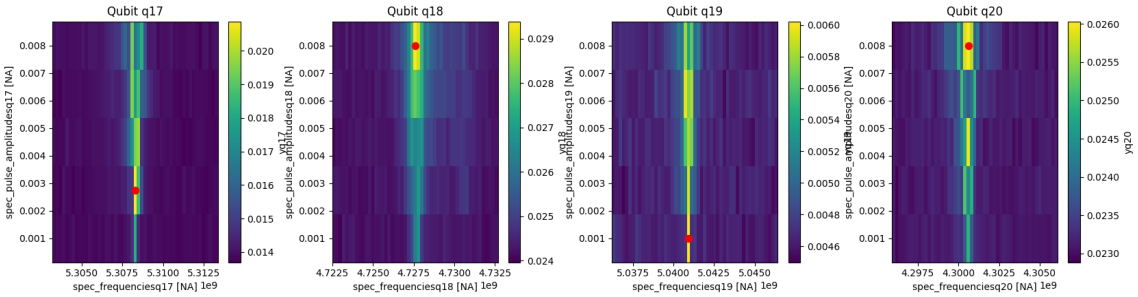


**Figure 4.4:** Results from the qubit spectroscopy. When the optimal qubit frequency is present, the resonator frequency shifts and a peak can be detected. The optimal amplitude is the amplitude that gives the largest peak.

### 4.1.3 Rabi Oscillations

After identifying the qubit transition frequency, the next step is to calibrate the amplitude of control pulses for single-qubit gates [33]. This is achieved through Rabi oscillation experiments. The qubit is driven at the resonance frequency with microwave pulses of varying amplitudes, and the qubit population is measured after each pulse.
The qubit undergoes coherent rotations on the Bloch sphere, and the measured population exhibits sinusoidal oscillations as a function of the drive amplitude [34]:

$$P_1(\Omega) = A \sin^2\left(\frac{\Omega T}{2}\right) + B, \tag{4.1}$$

where $\Omega$ is the scaled drive amplitude, $T$ is the fixed pulse duration, and $A$, $B$ are fit parameters accounting for contrast and offset. From the fitted curve, the amplitude corresponding to a $\pi$-pulse (which fully inverts the qubit from $|0\rangle$ to $|1\rangle$) is extracted. This calibration procedure is also performed starting from the $|1\rangle$ state to ensure the ability to excite the qubit to the second excited state.
To calibrate the amplitude of a $\pi$-pulse for single-qubit gate operations, Rabi oscillation measurements are performed. The schedule applies a fixed-duration DRAG pulse to each qubit at its respective transition frequency ($\omega_{01}$ or $\omega_{12}$), sweeping the

drive amplitude over a defined range, as shown in Figure 4.5. For transitions involving the $|1\rangle$ state, the qubit is initialized with an $X$ gate before the Rabi pulse. After each pulse, the qubit state is measured. The measurement is repeated multiple times (typically 1024) to obtain the average signal amplitude.

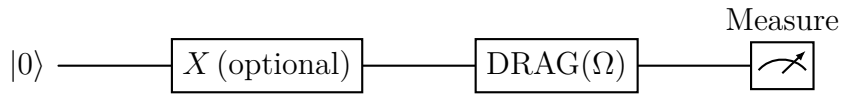


**Figure 4.5:** Pulse scheme for the Rabi oscillation calibration. The qubit is initialised to $|0\rangle$ by letting the qubit relax. If the experiment targets the $|1\rangle \rightarrow |2\rangle$ transition, a calibrated $X$ gate initializes the qubit in $|1\rangle$. A DRAG pulse with varying amplitude $\Omega$ is applied at the qubit transition frequency. The resulting qubit state is measured via the readout resonator.

Once the data is collected, it is analyzed by fitting a sinusoidal model to the measured signal as a function of drive amplitude. Initial parameter estimates are computed based on the amplitude range and signal shape. The model returns a best-fit curve and a parameter representing the amplitude corresponding to a $\pi$-rotation. The fitting also yields the uncertainty of this amplitude and computes a scaled uncertainty metric. If the scaled uncertainty is below a predefined threshold (e.g., $< 2\%$), the analysis is considered successful. The extracted $\pi$-amplitude is stored and used for calibrating control pulses in later experiments. The result is plotted together with the measured data points and fit curve, and the final calibrated amplitude is reported along with its uncertainty.

If the two previous measurements show good results, there usually is not to much problem getting good results for the Rabi oscillations. The measurement uses 61 points between the amplitude 2 mV to 900 mV. The data is fitted to an oscillating function and the peak with the lowest amplitude is used to perform the X-gate, see Figure 4.6. If half of the X-gate amplitude is calculated, this is the amplitude used to perform an X/2-gate [33]. Errors in the measurement could stem from either the resonator frequency or, more likely, the qubit frequency is not correctly calibrated. The data in that case does not follow an oscillating function. The code calculates the standard error and decides that with the $\pi$-amplitude to get the relative uncertainty. If the relative uncertainty is above 0.02, that is considered a bad fit.

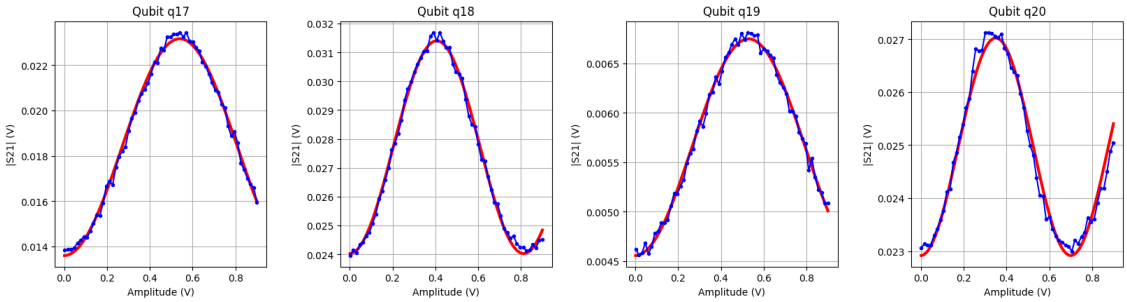


**Figure 4.6:** Rabi oscillations for the 01 transition. As the drive amplitude increases, the qubit undergoes coherent transitions between the ground and excited states, exhibiting periodic population oscillations. The optimal amplitude for a $\pi$-pulse corresponds to the first maximum of the fitted curve, where the qubit is fully excited to the $|1\rangle$ state.

### 4.1.4 Ramsey correction

To detect and correct for frequency detuning in each qubit, a series of Ramsey experiments with artificially introduced detunings is performed. For each value of the detuning parameter, a standard Ramsey sequence is executed, consisting of two $\pi/2$ pulses separated by a fixed delay $\tau$, during which the qubit accumulates a phase offset relative to the rotating frame of the drive [33], shown in figure 4.7.

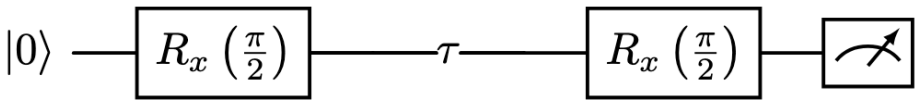


**Figure 4.7:** Ramsey sequence used for frequency detuning correction. The qubit is initialized in the ground state by relaxing the qubit and subjected to a $\pi/2$ pulse, followed by a delay $\tau$ during which the qubit accumulates a phase relative to the drive due to an artificial detuning. A second $\pi/2$ pulse completes the Ramsey sequence, and the final state is measured. The results, repeated for various detunings, enable calibration of the qubit's true resonance frequency.

The measurement assigns pulse configurations based on whether the $0 \rightarrow 1$ or $1 \rightarrow 2$ transition is being probed. For each qubit, data is collected over a grid of delay values and artificial detunings [35], with every configuration executed over multiple repetitions.
This process yields a set of fitted detunings as a function of the known artificial detunings. The point where the fitted detuning crosses zero gives the optimal frequency correction for the qubit, the value at which the applied drive is truly resonant. This correction is interpreted as the actual frequency offset from the qubit's transition frequency due to environmental shifts, residual miscalibration, or crosstalk effects.

With the Ramsey correction, the goal is to get a more accurate value for the qubit frequencies. This is done by applying some artificial detuning in the range of -2 MHz to 2 MHz. From these ranges, 6 points are collected. By fitting the values to a linear fit, one can see how off the qubit frequencies are and correct them accordingly, see Figure 4.8. If the points follow the linear fit, the calibrations have been right so far. If the points deviate too far from the fit, it could mean that there are still some errors that have not been discovered.

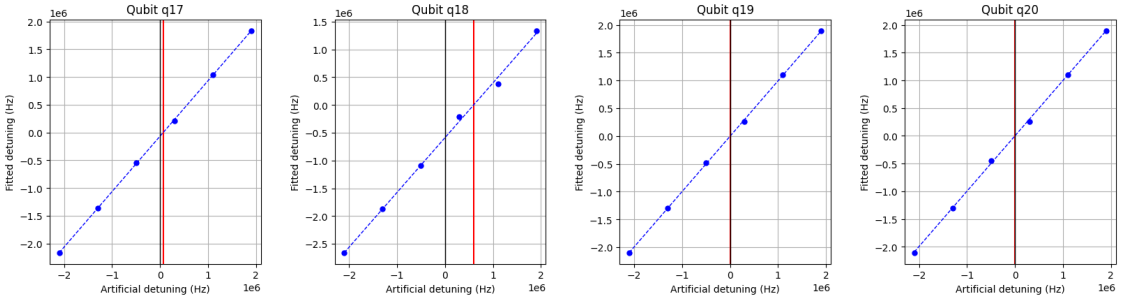


**Figure 4.8:** Results from Ramsey detuning calibration for the 01 transition. The fitted detuning is plotted against the applied artificial detuning, showing a linear relationship used to correct frequency offsets. The black vertical line indicates zero detuning, while the red vertical line marks the point of zero fitted detuning, revealing the required frequency correction to align the qubit with its true resonance.

### 4.1.5 DRAG (Motzoi) Calibration

The Dispersive Readout with Adiabatic Gate (DRAG) technique, introduced by Motzoi et al. [36], mitigates leakage to higher transmon levels (e.g., $|2\rangle$) during fast gates [7]. Because the transmon is only weakly anharmonic, a simple Gaussian pulse can excite non-computational states. DRAG solves this by adding a derivative component to the control pulse [37]:

$$\Omega(t) = \Omega_0(t) + i\beta\frac{d\Omega_0(t)}{dt}, \tag{4.2}$$

where $\Omega_0(t)$ is the in-phase Gaussian envelope, and $\beta$ is a tunable parameter controlling the quadrature correction. DRAG calibration involves sweeping $\beta$ and minimising leakage to $|2\rangle$ or oscillations in population that indicate imperfections. The calibration is applied for gates on both $|0\rangle \rightarrow |1\rangle$ and $|1\rangle \rightarrow |2\rangle$ to ensure leakage is suppressed in both directions.
For each qubit, a parameter sweep over multiple Motzoi values is defined to fine-tune the $\pi$-pulse. These values correspond to the weight of the derivative component in the DRAG pulse. The measurement schedule includes repeated application of DRAG and inverse DRAG pulses, followed by a qubit readout, see Figure 4.9. The number of DRAG repetitions is varied to amplify small errors and enhance sensitivity to leakage and overrotation. For each Motzoi value, the pulse sequence is applied multiple times to collect statistically significant data. The qubit state is then measured using either the standard dispersive readout or a state-specific readout. The full experiment is run for a range of Motzoi parameters and DRAG pulse

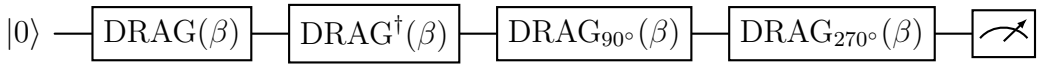


**Figure 4.9:** Pulse sequence for Motzoi (DRAG) parameter calibration. After letting the qubit relax to $|0\rangle$, a series of DRAG pulses with quadrature correction $\beta$ are applied, including standard and inverse pairs to enhance sensitivity to leakage. For $|0\rangle \rightarrow |1\rangle$ calibration, additional phase-shifted pulses (90° and 270°) are included to detect subtle leakage paths. The qubit is then measured to extract population dynamics as a function of $\beta$, enabling fine-tuning of the DRAG coefficient for optimal leakage suppression.

repetitions.
The corresponding analysis pipeline processes the measurement results to extract the optimal Motzoi parameter. The recorded signal magnitudes are reshaped into a two-dimensional dataset indexed by Motzoi value and repetition count. For each Motzoi parameter, the magnitudes are summed across all repetitions. The Motzoi value corresponding to the minimum total signal is selected as optimal. This approach assumes that the lowest measured signal indicates minimized leakage or coherent build-up.
The Motzoi parameter is swept between −0.4 to 0.1 and collecting 51 points. In addition, the number of times the DRAG-pulse scheme is applied, 3 of these repetitions are selected from a range of 1 to 19. The code then selects the Motzoi parameter that minimizes the sum of magnitude over all repetitions. This is easy to identify by eye, by looking at the dotted line that crosses a blue area in Figure 4.10. If this is the case, then the calibration has succeeded.

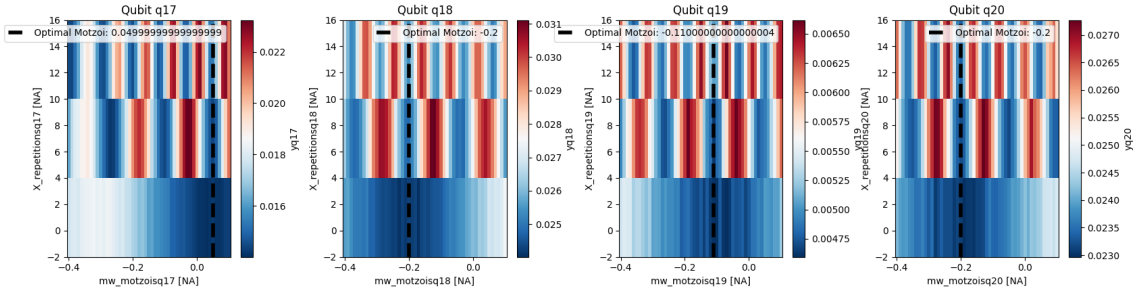


**Figure 4.10:** DRAG (Derivative Removal by Adiabatic Gate) calibration results. The DRAG technique, introduced by Motzoi et al.[36], mitigates leakage to higher transmon levels (e.g., $|2\rangle$) during fast gate operations by adding a quadrature correction to the control pulse. Each heatmap shows the dependence of qubit error signal on $\beta$ (horizontal axis) and the number of DRAG-pulse schedule repetitions (vertical axis), named X-repetition. The dark dashed lines indicate the optimal $\beta$ values which minimize leakage or population oscillations.

### 4.1.6 n-Rabi Calibration

The n-Rabi experiment generalises the standard Rabi experiment by applying $n$ sequential pulses (e.g., $n$ $\pi$-pulses) and observing the cumulative rotation effects,

see pulsescheme in Figure 4.11. This is useful for fine-tuning the pulse amplitude when small errors accumulate over repeated applications [33]. Ideally, the qubit should flip back and forth between $|0\rangle$ and $|1\rangle$, and any drift or decay in amplitude indicates over- or under-rotation or decoherence.

By comparing the experimental population oscillations with simulations, the n-Rabi sequence allows for precise correction of systematic errors in pulse calibration. It is especially effective for detecting small calibration mismatches not evident in single-pulse Rabi experiments.

The goal of this experiment is to identify and correct systematic calibration mismatches in the amplitude of the DRAG-pulses. This is achieved by executing sequences of multiple pulses and measuring the resulting state population after each sequence. The measurement strategy can be applied to both the $|0\rangle \leftrightarrow |1\rangle$ and $|1\rangle \leftrightarrow |2\rangle$ transitions by toggling the target qubit state.

The scheduling function builds the sequence by first applying a reset to all qubits by letting them relax to $|0\rangle$. Then, for each qubit, it loops over a sweep of microwave amplitude corrections and a series of repetition counts, generating pulse pairs for each combination. Each pulse pair includes a DRAG pulse and its counterpart, with a phase shift of 90° for quadrature correction if operating in the $|0\rangle \leftrightarrow |1\rangle$ manifold. The amplitude correction is applied by modifying the base amplitude retrieved from the transmon configuration. Finally, the measurement is taken.

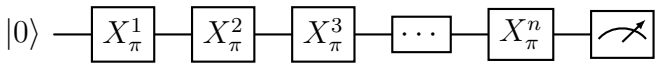


**Figure 4.11:** n-Rabi calibration sequence applying $n$ consecutive $\pi$ pulses to the qubit initialized in $|0\rangle$. This sequence amplifies systematic pulse errors by accumulating over- or under-rotations and decoherence effects over multiple $\pi$ pulses.

For each amplitude setting, the total signal magnitude is measured across all repetitions. The amplitude that yields the minimum total magnitude is presumed to be the most accurately calibrated value, corresponding to the most coherent destructive interference from cumulative rotations—i.e., closest to a full $2\pi n$ rotation returning the qubit to its initial state.

This amplitude shift is then used to compute a corrected $\pi$-pulse amplitude by summing the original calibrated amplitude with the offset determined from the n-Rabi analysis.

The n-Rabi procedure is close to the procedure for Motzoi calibration. Now the amplitude is swept from the ranges -0.045 mV to 0.045 mV and measuring 40 points. On the Y-axis, the number of X pulse repetitions varies from 1 to 19, but 3 equally spaced points are used. This is to correct the X-pulse amplitude, especially when the Motzoi parameter is taken into account. The analysis of the plot follows the same idea as for the Motzoi parameter, where the dotted black line should overlap blue regions, see Figure 4.12.

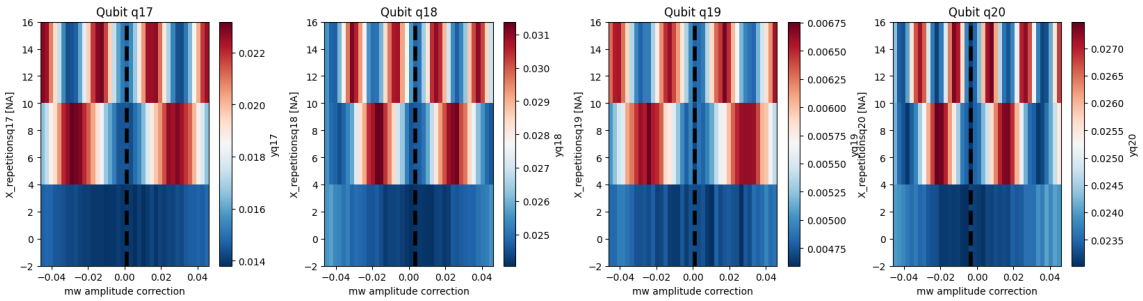


**Figure 4.12:** n-Rabi experiment results. The heatmaps show excitation probabilities as a function of microwave amplitude correction and the number of sequential $\pi$-pulses. This method enhances pulse calibration by amplifying small systematic errors that accumulate over repeated gate applications.

### 4.1.7 Resonator 1 Spectroscopy

For resonator spectroscopies at higher states, the frequency of the resonator changes, as anticipated, see Figure 4.13. This demonstrates the importance of accurately setting the initial resonator frequency. Misalignment can result in other frequencies falling outside the spectroscopic range, potentially causing miscalibration or fitting errors.

One other possible error that can occur is if the calibrations from the $|0\rangle$ state are not calibrated well. If there is an issue with going to the $|1\rangle$ state, the resonator spectroscopy for the higher states will not deliver accurate results. This can easily be spotted by human eyes by detecting no movement of the resonator frequency. No implementation in the code is done to automatically detect this error, so observing the plots is still highly relevant.

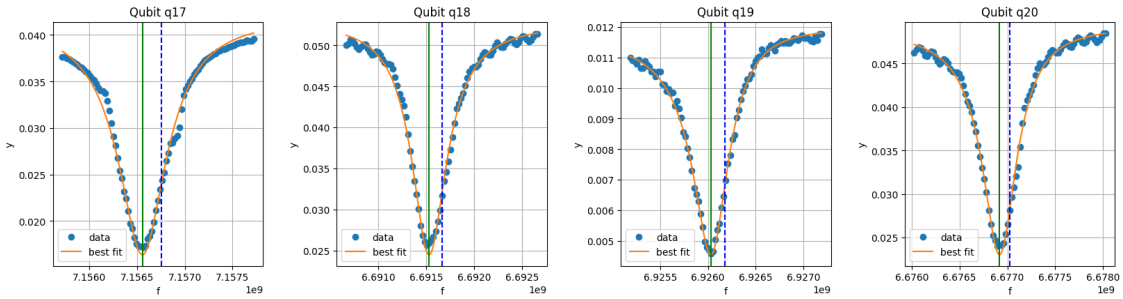


**Figure 4.13:** Resonator spectroscopy when qubits are in $|1\rangle$. The dip in the transition can clearly be seen, and the movement of the resonator spectroscopy can be detected. The green line shows the resonator frequency for the $|1\rangle$ state, and the blue dotted line shows the $|0\rangle$ state resonator frequency.

### 4.1.8 Qubit 12 Spectroscopy

The spectroscopy of a qubit in the $|1\rangle$ state is quite similar to that in the $|0\rangle$ state 4.14. Provided that the attenuation and measurement pulse amplitude are accurately configured, no further adjustments are required, as both state measure-

ments use the same amplitude. As noted above, errors might arise if the $|0\rangle$ state calibrations are not performed accurately, leading to an unaltered qubit frequency. To identify this issue, it is necessary to compare the two plots side by side to check for any frequency shifts. Detection of this error is possible through resonator spectroscopy, so examining those results can provide a reliable indication of such an error.

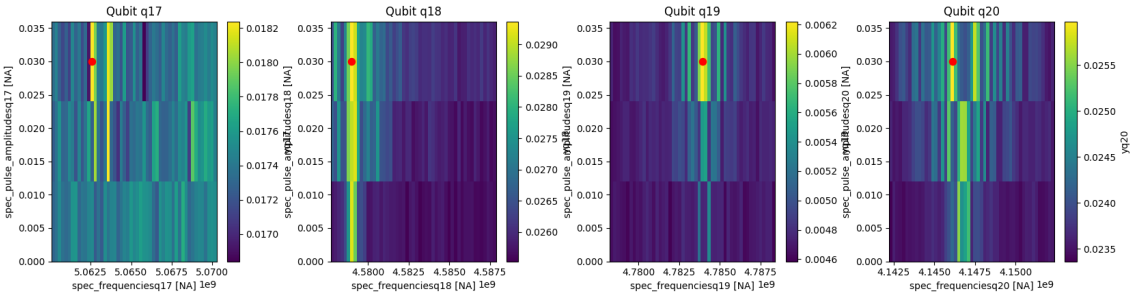


**Figure 4.14:** The results from qubit spectroscopy for the $|1\rangle$ state looks similar to the previous qubit spectroscopy measurement. The data is not as clear, but good results are still achievable.

### 4.1.9 Rabi 12 Oscillations

For Rabi oscillations between the $|1\rangle$ and $|2\rangle$ states, the procedure is exactly the same as in chapter 4.1.3 but instead of initizalizing the qubit to $|0\rangle$ it is now first excited to $|1\rangle$. Now the interesting parameter is the amplitude required to get to the $|2\rangle$ state shown in Figure 4.15.

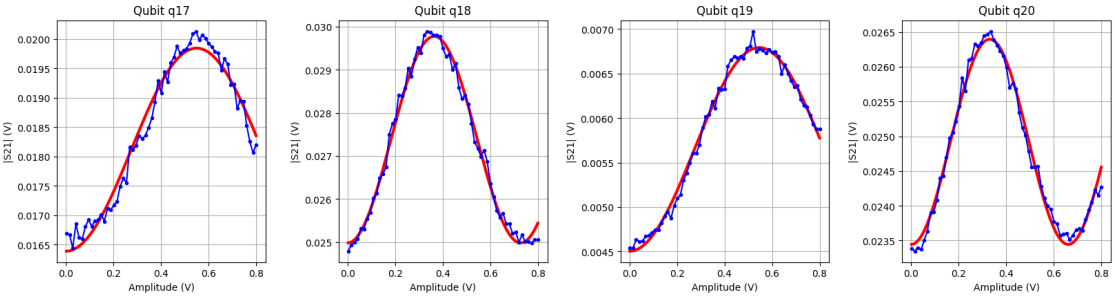


**Figure 4.15:** Rabi oscillations for the 12 transitions.

### 4.1.10 Ramsey 12 correction

For Ramsey correction between the 12 transition, the procedure is exactly the same as in chapter 4.1.4, but instead of initizalizing the qubit to $|0\rangle$, it is now first excited to $|1\rangle$. The results are presented in Figure 4.16.

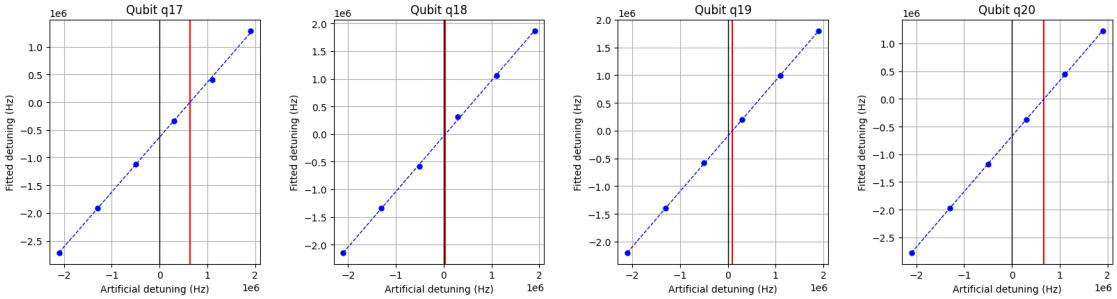


**Figure 4.16:** The results from the Ramsey fringes calibration. Uses the same principle as the 01 calibration, but now, the qubit is first excited before any measurements are taken.

### 4.1.11 DRAG (Motzoi) 12 Calibration

For Motzoi calibration for the $\pi$-pulse for the 12 transistion, the ranges change a bit. The Motzoi parameter is now swept between $-0.3$ and 0.3, still collecting 51 points. The DRAG schedule repetitions are between 1 and 4, and 3 of these are measured, see Figure 4.17. Here, as usual, the qubit is first excited before starting the measurement

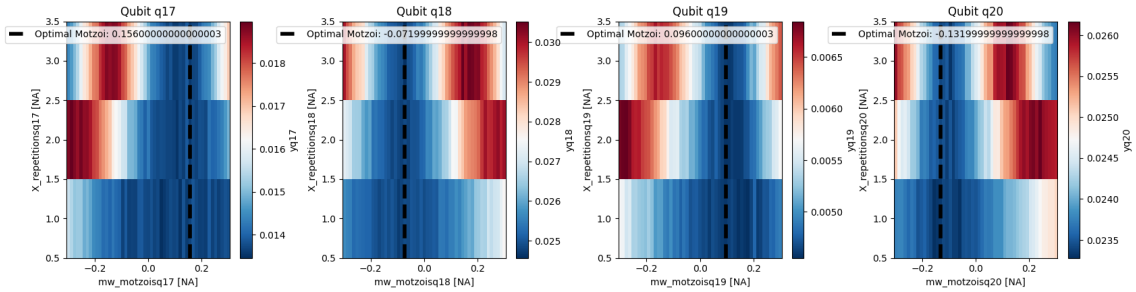


**Figure 4.17:** Plots show the results for calibrating the Motzoi parameter for the $\pi$-pulse for the 12 transition. Each heatmap shows the dependence of qubit error signal on $\beta$ (horizontal axis) and the number of DRAG-pulse schedule repetitions (vertical axis), named X-repetition. The dark dashed lines indicate the optimal $\beta$ values which minimize leakage or population oscillations.

### 4.1.12 Resonator 2 Spectroscopy

To perform the resonator 2 spectroscopy, the qubit is excited to $|2\rangle$ ahead of a standard resonator spectroscopy. The results are presented in Figure 4.18.

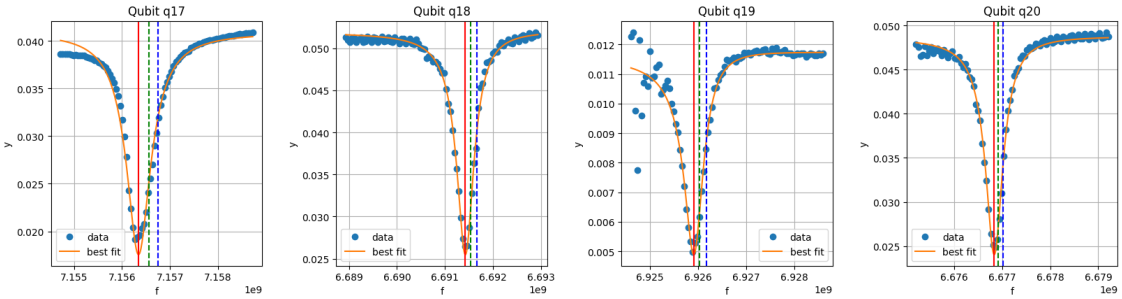


**Figure 4.18:** Resonator spectroscopy when the qubits are in $|2\rangle$. The new red line shows the resonator frequency for the $|2\rangle$ state.

## 4.2 Robustness of resonator and qubit frequencies

An interesting aspect to look at is how much the different frequencies change after each cool-down of the dilution refrigerator in which the quantum processing unit (QPU) is operated. The QPU includes physical computational qubits, control circuits, and traditional computing hardware for controlling and amplifying input and output signals, storing instructions in memory, and distinguishing signals from noise. There are several causes that can force the stopping operation and bring the fridge back to room temperature; general maintenance is a common cause, but it is also required in case the QPU is affected by trapped currents. To do this efficiently, it is important that the ranges that are swept are large enough that shifts in the frequencies can be accounted for. Four cool-down occurred during the period of this thesis and each time dedicated data was collected to measure the shifts.

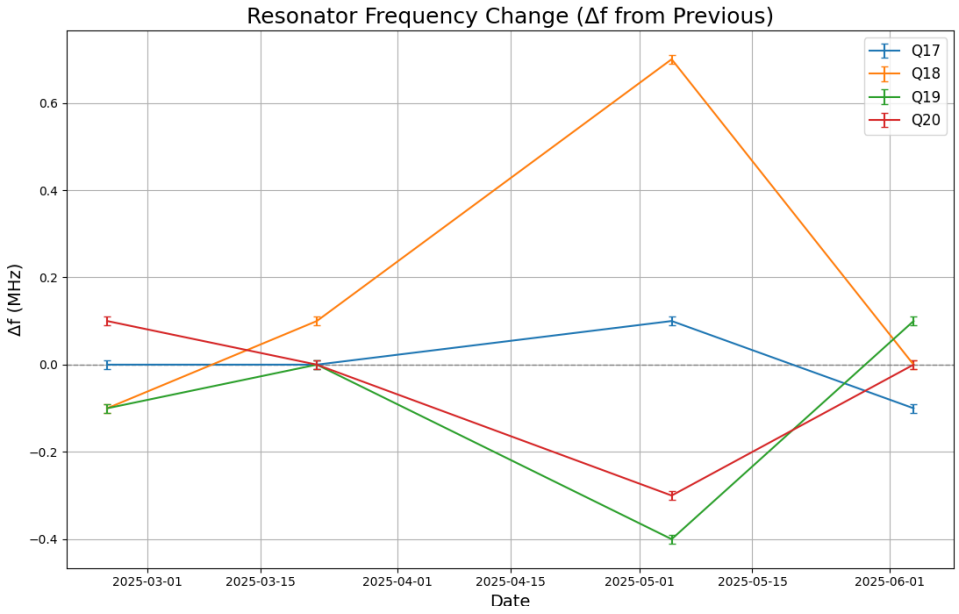


**Figure 4.19:** Changes in the resonator frequency compared to the first data point. The error bars are set to 10 kHz resulting in the maximum deviation 800 kHz

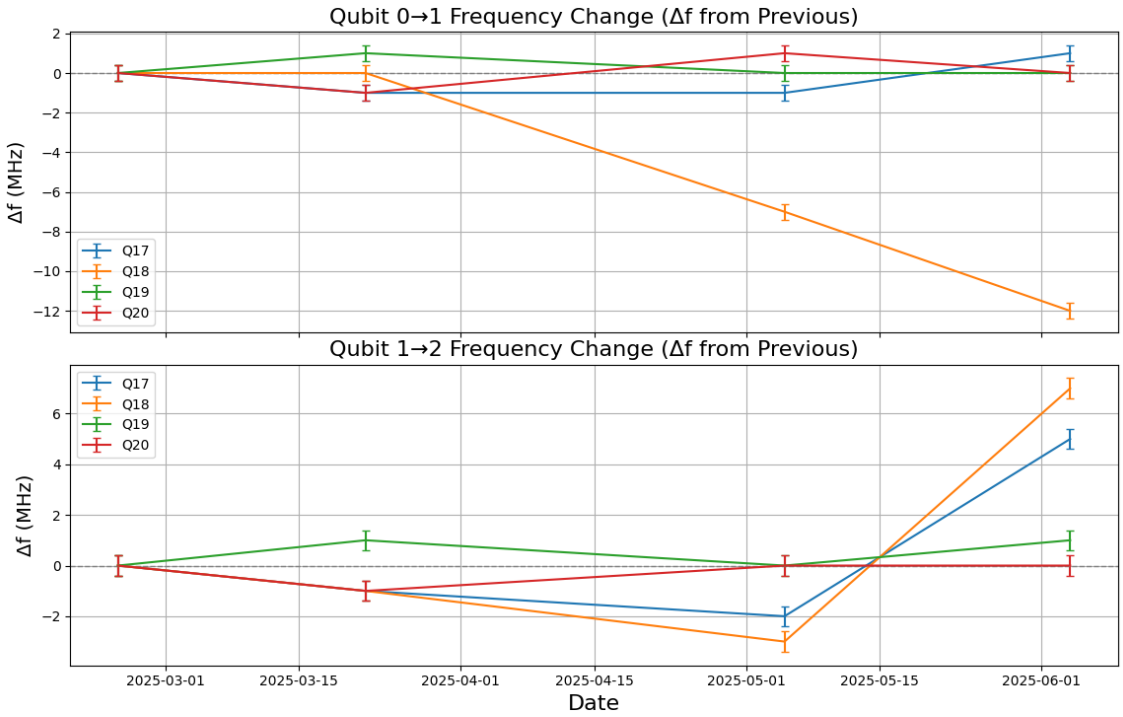


**Figure 4.20:** Frequency shifts for the $0 \rightarrow 1$ and $1 \rightarrow 2$ transitions. The error bars are set to 400 kHz. The largest shift 12 is for the $0 \rightarrow 1$ transition.

In this study, q16 was also included to increase the statistics, presented in Figure 4.19. The resonator frequency changes up to 0.8 MHz with an error of 10 kHz from propagation of error of the fitted frequencies. A sweep range for resonator spectroscopy of ±1.5 MHz is therefore enough to detect any shifts.

The qubit frequency is more prone to changes between temperature cycles, as presented in Figure 4.20. The maximum frequency shift is 12 MHz with an error of 400 kHz given by the granularity of the measurement. A range to ±20 MHz is enough to detect any frequency shifts. The maximum change for qubit 12 spectroscopy between one temperature cycle was around 7 MHz, so ±20 MHz satisfies the frequency changes for qubit 12 spectroscopy as well.

## 4.3 Readout Frequency and Amplitude Optimization

In superconducting qubit architectures, readout is typically achieved by coupling each qubit to a readout resonator, which reflects signals whose phase and amplitude depend on the qubit state. The discrimination of qubit states requires precise tuning of both the readout amplitude and frequency. This is performed within the node readout frequency and amplitude optimization. These results will give information that will be used for single-shot-readout (SSRO). SSROs are used when trying to distinguish between multiple states. After the calibration step is completed, one can perform SSRO measurements.

### 4.3.1 Readout Frequency Optimization

Readout frequency optimization is an important step in the context of dispersive readout schemes. In these systems, qubit state information is extracted via the interaction between a qubit and its associated resonator, whose response in the complex plane varies depending on the qubit's energy level. Optimal readout frequencies are chosen such that the difference in the resonator's response is maximized for different qubit states. This optimization directly enhances qubit state distinguishability and thus the fidelity of quantum measurements [33].

To perform this calibration step, square readout pulses at multiple frequencies across a predefined sweep range are applied. The qubit is prepared in the energy eigenstates $|0\rangle$, $|1\rangle$ and $|2\rangle$ to evaluate the frequency-dependent response of the readout resonator for each state [38]. Each of these preparations is followed by a pulse that performs a single-sideband demodulation and integrates the resulting complex signal over a square time window, storing the result as a complex-valued measurement used to read out qubit states. The measured response is tagged with an acquisition index and channel for identification during the analysis stage.

To analyse the resonator response traces are extracted for each qubit state from the acquired $S_{21}$ data and calculate state-specific magnitudes and phases. The $S_{21}$ responses of the three states form a triangle in the complex plane, and the area of this triangle is computed as a function of frequency using Heron's formula. The frequency that maximizes this triangle's area is then selected, ensuring maximal separability among all three states.

These optimization strategies are essential to achieving high-fidelity qubit readout, particularly in multiplexed setups where frequency crowding can introduce crosstalk and signal degradation. By ensuring that the readout resonator is probed at a frequency where the states are maximally distinguishable in the IQ plane, this calibration step mitigates measurement errors and supports robust quantum information processing in larger systems.

The outcome of the readout frequency optimization procedure is illustrated in Figure 4.21, which shows the IQ distance as a function of readout (RO) frequency. For each qubit, three traces represent the measured IQ distance corresponding to the qubit being prepared in the $|0\rangle$, $|1\rangle$, and $|2\rangle$ states. These traces highlight the frequency-dependent variation of the resonator response for each state, with well-defined dips indicating increased distinguishability.

Beneath each set of IQ distance curves, the red dashed line depicts the area formed by the triangle connecting the centroids of the three IQ distributions. This area is computed as a function of frequency using Heron's formula and serves as a quantitative proxy for the distinguishability of the three states in the IQ plane. The frequency at which this area is maximized (indicated by a red star) is selected as the optimal readout frequency for the corresponding qubit.

Across the twelve qubits analyzed, optimal frequencies were found in the range of approximately 6.5 GHZ to 7.1 GHz. All the qubits exhibit well-separated and deep minima in their IQ distance curves, indicating strong contrast among states.

These results validate the effectiveness of using the triangle area metric for frequency optimization, particularly in systems with three-level readout. Selecting frequencies based on this metric ensures maximal state separation in the IQ plane, thus enhanc-

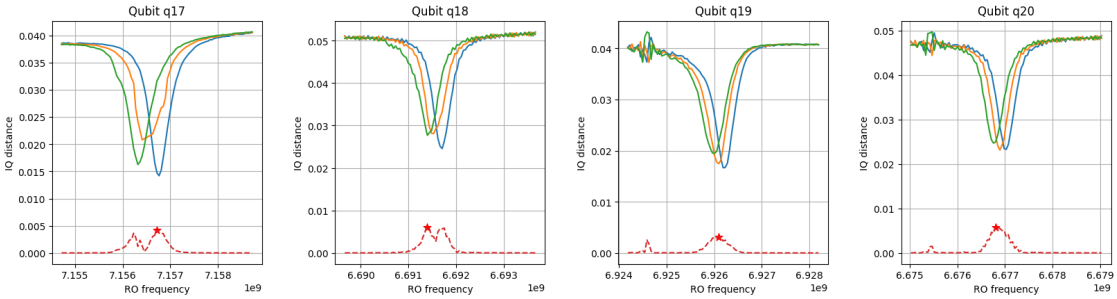


**Figure 4.21:** Readout frequency optimization results. Each subplot shows the IQ distance versus RO frequency for states $|0\rangle$, $|1\rangle$, and $|2\rangle$. The red dashed curve indicates the triangle area metric, with the optimal frequency marked by a red star.

ing measurement fidelity.

### 4.3.2 Optimal Readout Amplitude Calibration

Optimizing the amplitude of the readout pulse is essential for maximizing the signal-to-noise ratio in the dispersive readout of superconducting qubits. This calibration aims to determine the amplitude that produces the most distinguishable measurement outcomes between different qubit states while avoiding distortion or nonlinearities in the resonator response.

The calibration proceeds by sweeping the amplitude of the square readout pulse across a predefined range. At each amplitude, the qubit is prepared in one of the energy eigenstates $|0\rangle$, $|1\rangle$, or $|2\rangle$. A square readout pulse is then applied to the resonator, and the signal is demodulated using single-sideband techniques and integrated to yield complex-valued IQ data [38]. Each measurement is indexed by both amplitude and state label for later analysis.

For each amplitude, a linear discriminant classifier is fit to the IQ data, and a confusion matrix is computed to quantify classification performance. The amplitude corresponding to the highest trace of the confusion matrix is chosen as optimal.

The analysis returns key parameters such as the optimal amplitude, rotation angle, and classification thresholds or boundaries, which are stored for use in subsequent runtime execution.

The results of the readout amplitude optimization are shown in Figure 4.22, which presents the outcome of sweeping the amplitude of the square readout pulse for a set of qubits. Each column in the figure corresponds to a different qubit, with three panels per qubit showing the fidelity curve, IQ data distributions, and confusion matrix.

In the top row, the assignment fidelity is plotted as a function of readout amplitude. The blue curve indicates the average fidelity achieved by a linear discriminant classifier trained to distinguish among the three prepared states $|0\rangle$, $|1\rangle$, and $|2\rangle$. The optimal amplitude (marked by an orange star) is selected as the amplitude that yields the maximum average fidelity [33].

The middle row shows the IQ plane distributions of the demodulated signals at the optimal amplitude. Each point corresponds to a single measurement, colored by the

prepared state. The classification boundaries learned by the discriminant analysis are also shown, illustrating how the IQ clusters for different states are separated. The centroids and decision vectors give insight into the separability and orientation of the measurement distributions.

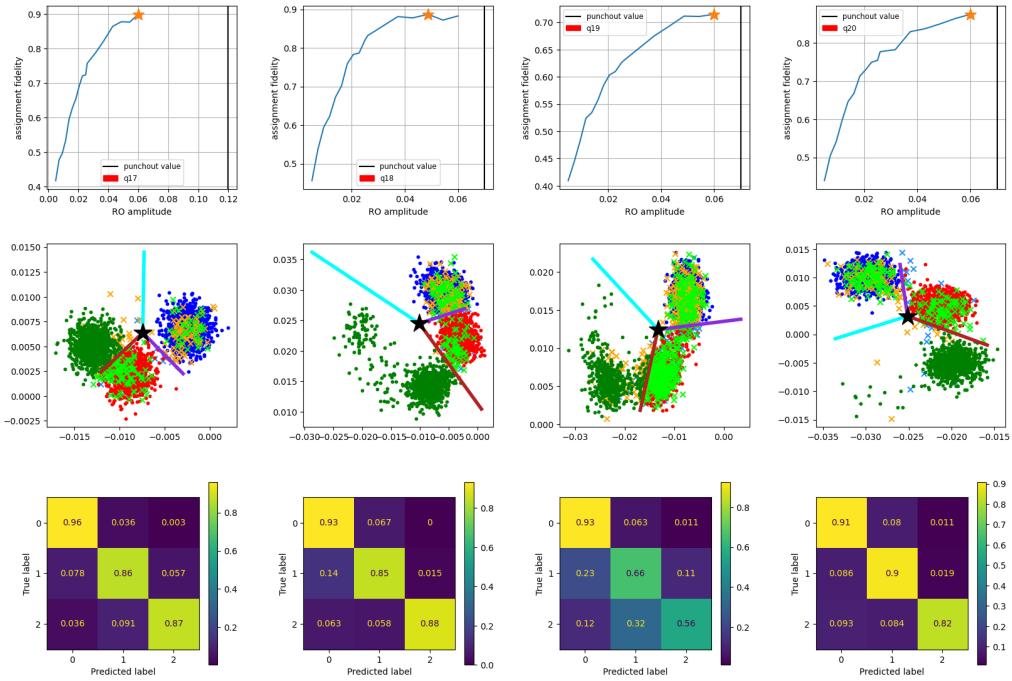


**Figure 4.22:** Readout amplitude optimization results for several qubits. Each column corresponds to one qubit. **Top row:** Assignment fidelity versus readout amplitude with the optimal amplitude marked by an orange star. **Middle row:** IQ distributions at the optimal amplitude with classification boundaries. **Bottom row:** Confusion matrices indicating classification performance for the three states $|0\rangle$, $|1\rangle$, and $|2\rangle$.

The bottom row displays the confusion matrices at the optimal amplitude. Each matrix element quantifies the probability of classifying a prepared state $i$ as a predicted state $j$. High values along the diagonal indicate successful classification, while off-diagonal elements represent state confusion and misclassification rates.

Across the set of qubits analyzed, the optimal amplitudes vary but consistently yield improved state distinguishability in the IQ plane. This optimization procedure ensures that the readout pulse is strong enough to produce well-separated state responses without introducing non-linearities or resonator distortions. The extracted parameters are optimal amplitude, rotation angle, and classification thresholds.

## 4.4 Gate performance evaluation: Randomized Benchmarking

Quantum computers operate through the coherent manipulation of qubits, using sequences of quantum gates. However, these gates are subject to various types of noise and imperfections, making the reliable characterization of gate fidelity a crucial task in quantum information processing. Among the various techniques developed to address this challenge, randomized benchmarking (RB) has emerged as a robust and scalable method to estimate the average error rate of quantum gates [39].
RB is fundamentally a statistical method that characterizes the average performance of a set of quantum gates drawn from the Clifford group [40], by applying sequences of randomly chosen gates followed by their inverses [39]. The key advantage of RB over full quantum process tomography lies in its efficiency and resilience to state preparation and measurement (SPAM) errors [41]. Rather than reconstructing the full process matrix of a gate, RB estimates the average fidelity over many gate sequences, allowing for the extraction of error rates with relatively low experimental overhead.
In the single-qubit case, the benchmarking procedure begins by initializing the qubit in a reference state, commonly the ground state $|0\rangle$. A sequence of $m$ gates is then applied, each drawn uniformly at random from the single-qubit Clifford group. These gates collectively form a unitary operator $C_m$. To invert the effect of the sequence, an additional Clifford gate $C_m^\dagger$ is appended such that, in the absence of noise, the entire sequence ideally returns the qubit to its initial state [42], illustrated in Figure 4.11. After the application of the sequence, the final state is measured in the computational basis. This process is repeated multiple times for various random sequences and for increasing sequence lengths $m$.

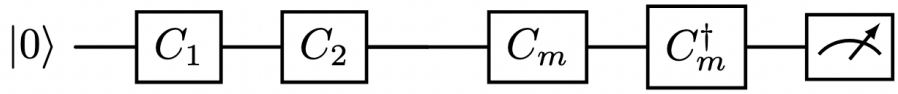


**Figure 4.23:** Single-qubit RB circuit. The qubit is initialized in the state $|0\rangle$, followed by a sequence of $m$ randomly selected Clifford gates. An additional gate $C_m^\dagger$ inverts the sequence. In the absence of noise, the qubit returns to $|0\rangle$. The final measurement is used to estimate the average gate fidelity.

The measurement outcome probabilities as a function of sequence length exhibit an exponential decay behavior, which can be modeled as $F(m) = Ap^m + B$, where $F(m)$ is the average survival probability, $p$ is related to the average gate fidelity, and $A$, $B$ are constants absorbing SPAM errors. The parameter $p$ is connected to the average error per gate via the relation $r = \frac{d-1}{d}(1-p)$ for a system of dimension $d$. For single qubits, $d = 2$, and the decay parameter $p$ provides a direct estimate of the gate fidelity.

Extending RB to two qubits involves additional complexity due to the larger Clifford group and the increased Hilbert space dimension. In the two-qubit case, the gates are drawn from the two-qubit Clifford group, which includes both single-qubit and two-qubit entangling gates such as the controlled-NOT (CNOT) [13]. The procedure is conceptually similar: a random sequence of two-qubit Clifford gates is applied to an initial product state $|00\rangle$, followed by the inverse of the composite sequence. Measurements are performed on both qubits, and the survival probability is extracted as a function of sequence length.
Two-qubit RB also exhibits an exponential decay of fidelity with sequence length, with the decay parameter now reflecting the combined probability over the two-qubit Clifford group. As in the single-qubit case, SPAM errors contribute only to the offset and scale of the decay curve, leaving the decay rate as a reliable estimator of gate fidelity. Moreover, two-qubit RB can be modified to isolate the performance of specific gate types, such as interleaved RB, which intersperses a target gate within each step of the sequence to assess its fidelity individually.
RB provides an estimate of gate fidelity by accounting for both coherent and incoherent errors, including those related to qubit decoherence characterized by the $T_1$ and $T_2$ times. This technique offers insight into how accurately quantum gates perform in practice and, by extension, how reliable quantum measurements will be when using these qubits.
In the benchmarking procedure, sequences of single-qubit Clifford gates are applied, with the sequence length increasing up to 1024 gates. The protocol is repeated four times. A critical requirement for valid benchmarking is that the population begins close to 1. If this condition is not met—i.e., if the qubit is not properly initialized into the ground state—then the measured fidelity will be artificially high, misrepresenting the actual gate performance.

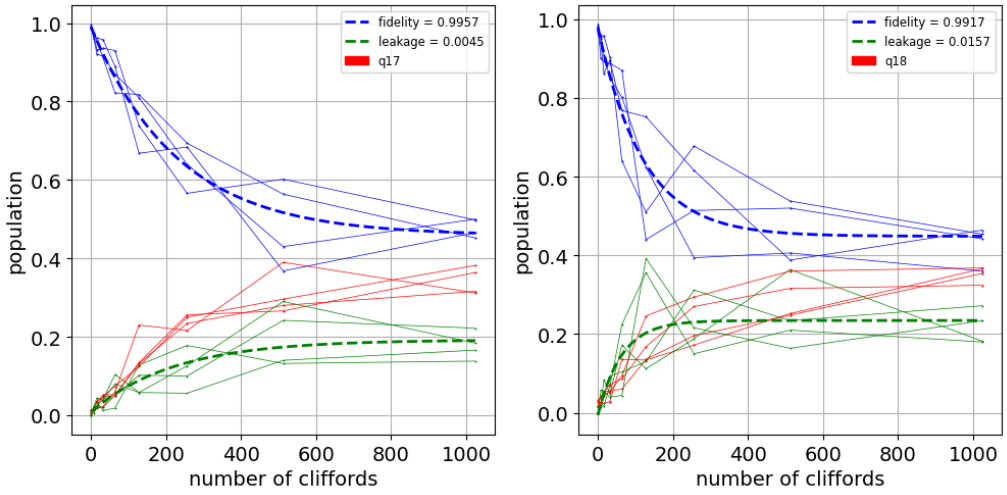


**Figure 4.24:** The RB measurement is shown above. The blue data is how the excited state varies in relation to the number of Clifford gates, the red data shows the ground state and finally the green depicts the higher energy states (leakage).

For this measurement, see Figure 4.24, qubit 17 achieved a high fidelity of approximately 0.996, which is considered acceptable. Qubit 18, on the other hand, showed

a slightly lower fidelity of 0.992. While not optimal, this result is still acceptable and indicates that both qubits were successfully initialized and excited during the benchmarking process. For some qubits, the qubit was never in the right state at the beginning of the measurement. Therefore, this performance is favourable compared to other qubit pairs where initialization errors were more pronounced.

## 4.5 Calibration of the CZ Gate

The controlled-Z (CZ) gate is a two-qubit gate, implementing a conditional phase shift such that the $|11\rangle$ state acquires a phase of $\pi$, while the other computational basis states ($|00\rangle$, $|01\rangle$, $|10\rangle$) remain unaffected, up to local phases [12]. This gate is essential for creating entanglement and enabling universal quantum computation. However, high-fidelity operation of the CZ gate necessitates a careful and systematic calibration procedure to avoid leakage into non-computational states and suppress spurious phase accumulation.

The CZ gate relies on a dynamical interaction mediated by a tunable coupler, which is modulated by a flux pulse. The effectiveness of the gate depends on the precise tuning of four parameters: **flux**, **frequency**, **amplitude**, and **duration** of the applied pulse [43]. These control the trajectory through the energy level landscape that enables the conditional phase interaction.

Since the frequency of the coupler is flux-dependent, one must characterize how it varies with the applied flux bias. Instead of performing direct spectroscopy on the coupler (which is not possible), it is possible to estimate the coupler frequency as a function of the flux by performing spectroscopy on the qubit and the resonator while sweeping the flux. When the coupler's frequency approaches the frequency of the qubit or resonator, an avoided crossing or level repulsion occurs, observable as distinct features in the spectra. These crossing points allow for the mapping of the coupler's flux-to-frequency dependence.

The optimal flux biases for CZ gates are chosen between the maximum of the two qubit frequencies and the minimum of the two resonator frequencies. At these operating points, frequency shifts of approximately $f_{12} - f_{01}$ ensure that the $|11\rangle$ state undergoes a nontrivial evolution while minimizing transitions to non-computational states [44].

Once candidate flux and frequency points are identified, the next step is to find the optimal flux and frequency point of the CZ pulse. A real-valued square pulse convolved with a Hann window is used for this purpose. The Hann window smooths the pulse's spectral profile, reducing spectral leakage and suppressing excitations outside the intended interaction path.

This pulse is tested by preparing both qubits in the excited state and applying the CZ interaction. Ideally, one of the qubits transitions to the ground state while the other reaches the second excited state, corresponding to a population transfer mediated by the $|11\rangle \leftrightarrow |02\rangle$ or $|20\rangle$ avoided crossing [45], see Figure 4.25. Successful population transfer indicates an effective entangling interaction and allows filtering out poor candidates and refining the CZ pulse.

Although the CZ gate is designed to only impart a $\pi$ phase to the $|11\rangle$ state, the gate also introduces **local dynamic phases** on the individual qubits due to detuning

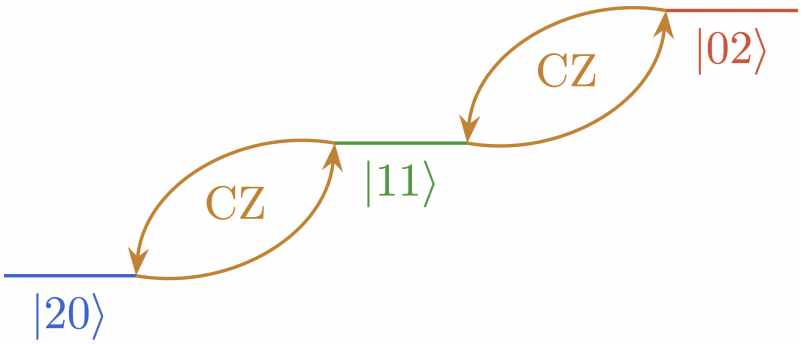


**Figure 4.25:** Level diagram illustrating the effective interaction path for a CZ-gate. The computational basis state $|11\rangle$ is coupled to the non-computational states $|20\rangle$ and $|02\rangle$ via higher-excited-state transitions, as indicated by the curved arrows labelled "CZ". While both transitions are theoretically accessible, only one of them (e.g., $|11\rangle \leftrightarrow |20\rangle$) is used in practice to mediate the search time for the optimal CZ-gate.

and interaction with the coupler. These local phases, if uncorrected, can accumulate over multiple gate operations and lead to coherence loss or logical errors in quantum algorithms.

To calibrate and compensate for these local phases the local phases have to be measured. A Ramsey-type interferometric sequence is applied to measure the single-qubit phase shifts induced by the CZ gate [13]. The target qubit's phase is then read out through Ramsey interference, and the resulting phase offset is extracted from the fringe pattern. These offsets are corrected via virtual Z gates.

This dynamic phase correction ensures that the gate behaves as a true controlled-Z operation in the computational subspace, free of unwanted single-qubit rotations [45]. Such corrections are essential in applications requiring high phase coherence, including variational algorithms and quantum error correction codes.

## 4.6 CZ Gate Calibration techniques

This section outlines the methods used to calibrate the CZ gate, a two-qubit gate that applies a conditional $\pi$ phase to the $|11\rangle$ state while leaving other computational states unchanged, aside from local phases.

The procedure presented here is a significant evolution from the calibration presented in [12, 46]. While the final steps of the CZ calibration are similar, the procedure is devised that allows it to determine the best bias flux that was instead empirically chosen in [12, 46]. In an automatic calibration of 40 couplers, there is no room for human intervention at the scale needed to select all bias points; instead, they need to be found procedurally and efficiently within a small amount of time. The work carried out provides this crucial component for the full calibration of the 25 qubit chip developed at Chalmers.

### 4.6.1 Principle of Operation

The CZ gate operates by dynamically modulating the frequency of a tunable coupler placed between two qubits. This is achieved via a flux pulse applied to the coupler, which temporarily adjusts its frequency to induce an interaction between the $|11\rangle$ computational state and non-computational states such as $|02\rangle$ or $|20\rangle$. A carefully timed and shaped flux pulse enables this avoided crossing to impart a conditional phase on the $|11\rangle$ state, realizing the entangling CZ operation.
As dicussed in Chapter 3.3 the couplers

### 4.6.2 Characterizing the Coupler

Since the coupler's frequency depends on the applied flux, the first step in the calibration procedure involves mapping its flux-frequency dependence. Rather than performing direct spectroscopy on the coupler itself. It would be preferred to perform coupler spectroscopy, but this cannot be done because the couplers do not have a dedicated readout resonator. The approach is instead to perform spectroscopy on the coupled qubit and resonator while sweeping the flux bias applied to the coupler. When the coupler approaches the frequency of either element, level repulsion or avoided crossings become visible in the spectrum. These features indicate points of strong coupling and allow the coupler's response to be indirectly characterized.

#### 4.6.2.1 Resonator spectroscopy as a function of the flux

Performing the resonator spectroscopy as a function of the flux is the same measurement and analysis as for the standard resonator spectroscopy. The flux varies between -1 mA to 1 mA with 50 $\mu$A steps. Why this step size is used will be discussed in section 4.6.3. Doing this will affect the resonator frequency as demonstrated in Figure 4.26. The flux values, where there is an abrupt change (switch) in the resonator frequency are the points at which the coupler has the same frequency as the resonator [33]. This point is called a crossing point. These points are used to attain the coupler's frequency as a function of flux.
For resonators with high frequencies, there exists no frequency switch (see top left plot in Figure 4.26). This means that the coupler will never have a frequency as high as that resonator. Detecting this point as a crossing point is not completely right, and perhaps not using that point could lead to better fits. No major disadvantage were discovered using this point as a crossing point in our final coupler frequency fit.
In most cases, the coupler frequency reaches the resonator frequency, and the switch is noticeable. To detect this in the analysis, the two points next to each other are compared, and if they are over a threshold of 2 MHz from each other, that flux point is said to be the crossing point. The analysis also includes a spurious threshold, meaning that the two data points around the point that is above the spurious threshold are compared. If the two data points are below that spurious threshold, the point is not detected as a crossing point. This eliminates the issue that bad data points can be wrongly detected as crossing points.

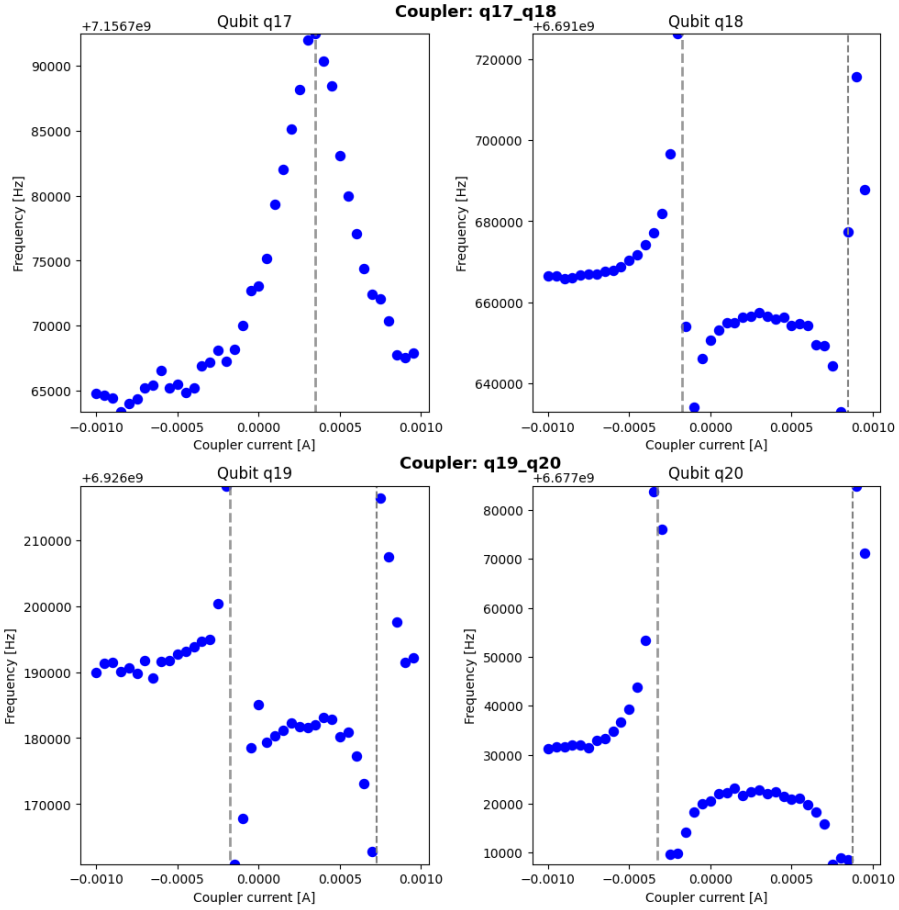


**Figure 4.26:** Resonator spectroscopy as a function of flux. Each blue point is the frequency of the resonator at the specific SPI current; these values are obtained from the fit of the individual resonator spectroscopies. The dashed lines show the estimated crossing points. The top left is for a resonator frequency that is above the limit of the coupler's frequency, and avoided crossing does not manifest. The rest of the plots behave as expected.

#### 4.6.2.2 Qubit spectroscopy as a function of flux

Qubit spectroscopy as a function of flux approach has the same approach as the standard qubit spectroscopy, with some important differences. Similarly to the flux-dependent resonator spectroscopy when, at certain values of flux, the coupler has the same frequency as the qubit, the qubit frequency will switch [47]. The sweep ranges are increased to -2.5 mA to 2.5 mA and still uses 50 $\mu$A steps.
This measurement differs from the standard qubit spectroscopy in that the amplitude is not swept. The optimal amplitude for the qubit spectroscopy is used for the entire measurement. If the analysis tries using a Lorentzian causes issues when the qubit frequency is close to the sweep range end points. When this occurs, the Lorentzian is no longer a good alternative for detecting the maximum point. Instead, an easy maximum point method is used to find the maxima. This resulted in significant improvements in the data and made detecting the crossing points a lot easier, see Figure 4.27.
The flux-dependent qubit spectroscopy analysis is based on the same idea as the resonator spectroscopy in subsection 4.6.2.1. Some extra steps are needed to get good crossing point detections. At these crossing points, significant noise affects the qubit spectroscopies, and no clear peak results in the maximum point detection chooses the maximum point of the dataset and sets that to the peak. To combat this, the maximum value is compared against the mean value plus 2.5 standard deviations. The 2.5 standard deviations were first just experimentally tested and proven to be a good estimation. If the maximum value is below the mean value plus 2.5 standard deviations, the data point is ignored. Doing this enables easy detection of the real crossing points.
To achieve a good coupler frequency fit requires no false positives. To combat this, the analysis only allows one crossing point in a 300 $\mu$ A region. This resolves the issue of the analysis detecting multiple crossing points in one crossing region.
When detecting crossing points, it is important that it does not detect a false crossing point, but if not all crossing points are detected, the fit still works fine. With all crossing points detected, the coupler can be characterized.

#### 4.6.2.3 Coupler Frequency Characterization

To determine the flux-to-frequency dependence of the coupler, we extract avoided crossings observed in both qubit and resonator spectroscopy as a function of the applied flux. These avoided crossings occur when the coupler becomes near-resonant with either a qubit or a resonator and manifest as distinct spectral features.
The combined set of crossing points is then fitted to a model function of the form [44]:

$$f_{\text{coupler}}(I) = f_c\sqrt{|\cos\left(\pi a(I-b)\right)|} + c, \tag{4.3}$$

where $f_c$, $a$, $b$, and $c$ are free parameters representing the coupler's maximum frequency, periodicity, offset, and baseline, respectively. This functional form captures the periodic cosine-like behaviour of the flux-tunable coupler.
From the fitted curve, candidate frequencies for the CZ gate are chosen as harmonic detunings from the difference of the qubit $|01\rangle$ and $|12\rangle$ transitions. These candidates are filtered to ensure that they lie below both resonator frequencies, thereby avoiding

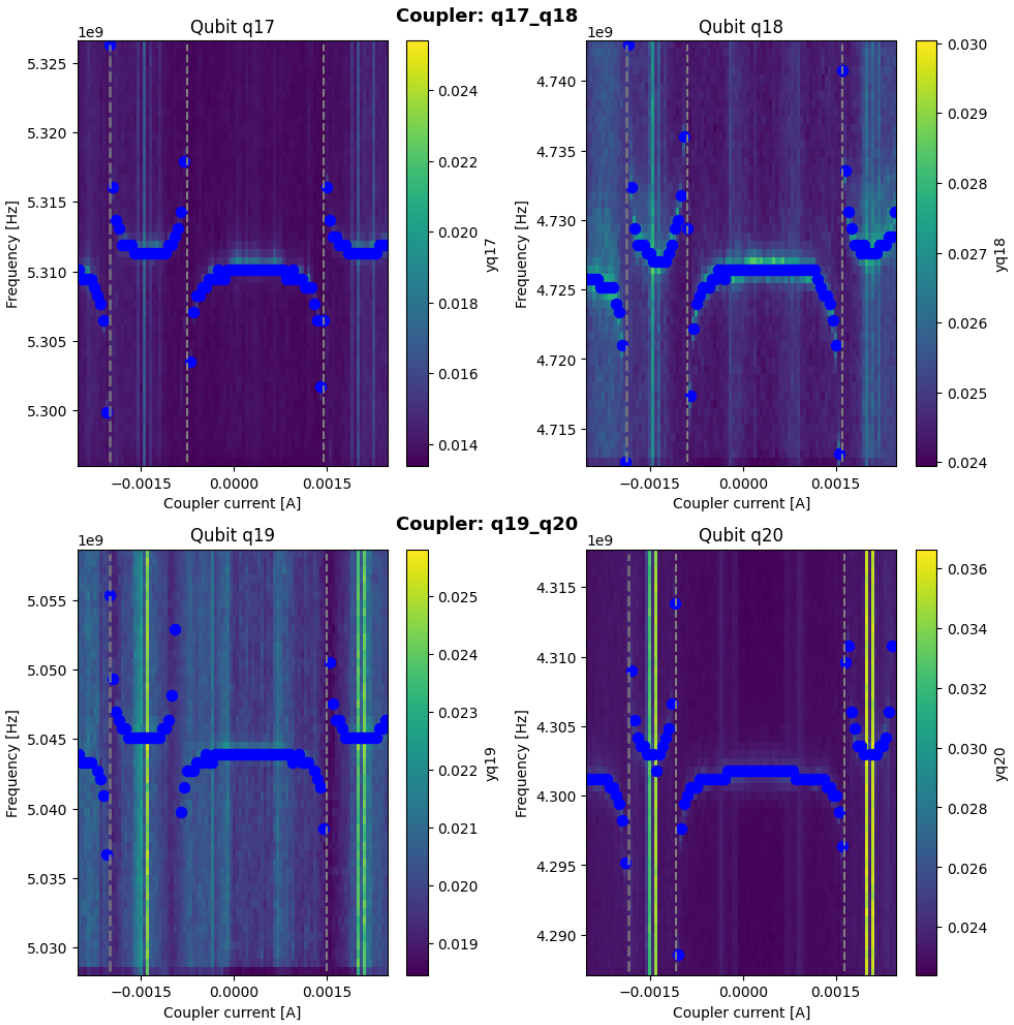


**Figure 4.27:** Qubit spectroscopy as a function of flux. Each column in the 2D plots shows the magnitude of a qubit spectroscopy with the blue point representing the selected frequency of the qubit. The vertical dash lines are the estimated crossing points.

leakage to unwanted states. The corresponding flux biases are then determined by solving the inverse of the fitted model.
All the necessary crossing points can be fitted to the model in Equation 4.3. This gives the plot shown in Figure 4.28. The fit works well, and now the coupler frequency has been characterized. To choose suitable candidates for the CZ-gate points between the highest qubit frequency and lowest resonator frequency are chosen with $|f_{01,q1} - f_{12,q2}|$ intervals. This gives 8-12 flux points that will be tested for candidates for the CZ-gate.

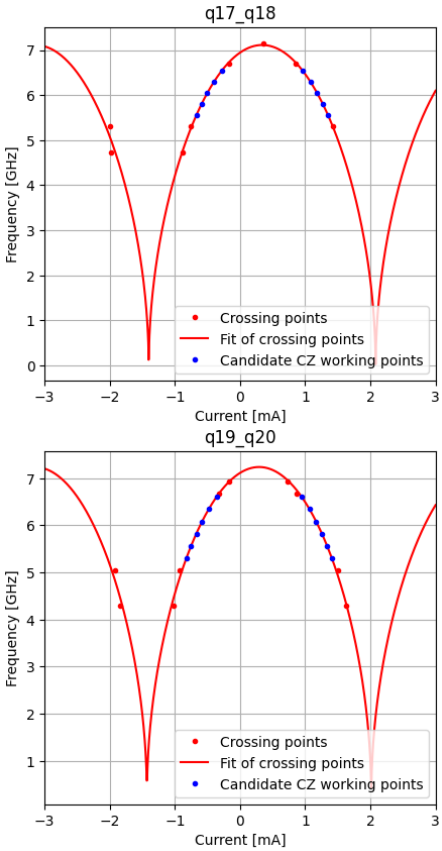


**Figure 4.28:** Inferred coupler spectroscopy for two couplers. The crossing points are shown in red, and the fitted coupler frequency as a red line. The blue points are the candidates for the CZ-gate.

### 4.6.3 Study of stepsize

As discussed in subsections 4.6.2.1 and 4.6.2.2, the stepsize for resonator and qubit spectroscopy as a function of the fluxi s chosen to be 50 $\mu$A. A study was conducted that looked at how much the CZ-candidates would change when the stepsize for the flux-dependent spectroscopies was changed. This is relevant because the flux-dependent spectroscopies take close to an hour; if smaller stepsizes are used, the time can decrease massively. So a base of stepsize 20 $\mu$A was set as a "perfect value" and then the stepsize was increased and the deviation from the baseline was studied. It was discovered that using a 50 $\mu$A stepsize still resulted in a maximum deviation

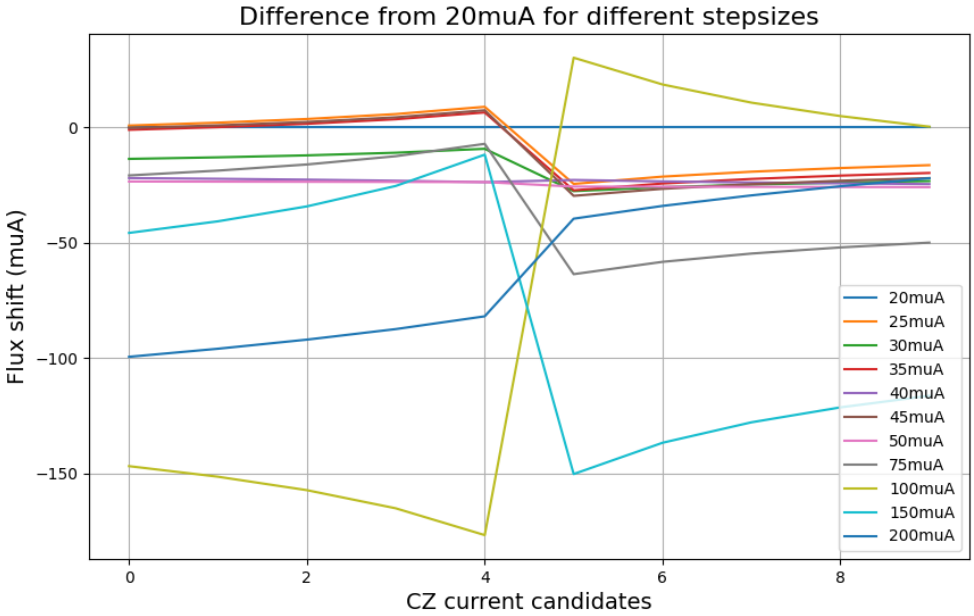


**Figure 4.29:** Deviation for the possible CZ-current points compared to the 20 $\mu$A stepsize. The 20 $\mu$A stepsize is zero along all values.

of 25 $\mu$A for all the current candidates, results in Figure 4.29. This was considered "close enough" and by coming down from 20 $\mu$A stepsizes decreases the measurement time by around half. This is a major time loss when the original measurement takes around one hour.

### 4.6.4 CZ parametrization with fixed duration

With candidate operating points identified, the next step is to implement and calibrate the flux pulse that mediates the CZ interaction. A square pulse convolved with a Hann window is employed to suppress spectral leakage and mitigate unwanted transitions, see pulse scheme in Figure 4.30. The Hann window smoothly ramps the pulse on and off, thereby confining its spectral bandwidth and minimizing overlap with non-targeted energy levels.

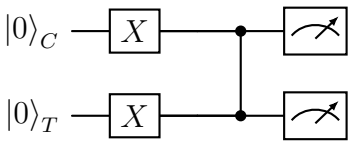


**Figure 4.30:** Circuit representation of the CZ parametrization experiment. Both qubits are initialized to the excited state, then a CZ-gate with half of the CZ-gate duration is applied with a frequency and amplitude sweep. Finally the states of the qubits are measured.

This shaped flux pulse is applied to the coupler while both qubits involved in the

interaction are initialized in their first excited state. When the coupler frequency approaches the avoided crossing associated with the $|11\rangle \leftrightarrow |02\rangle / |20\rangle$ transition, population transfer into these higher excited states can occur. The observation of such transitions serves as a signature of successful coupling and validates the alignment of the pulse parameters with the intended interaction point. These measurements thus guide further refinement of pulse amplitude, frequency, and timing for high-fidelity CZ gate implementation.
This shaped flux pulse is applied to the coupler while both qubits involved in the interaction are initialized in their first excited state. When the coupler frequency approaches the avoided crossing associated with the $|11\rangle \leftrightarrow |02\rangle / |20\rangle$ transition, population transfer into these higher excited states can occur. The observation of such transitions serves as a signature of successful coupling and validates the alignment of the pulse parameters with the intended interaction point.
The analysis begins by systematically exploring the parameter space defined by the coupler's parking currents, pulse frequencies, and amplitudes. For each parking current, the algorithm conducts scans to analyze frequency against amplitude for both qubits, pinpointing the maximum and minimum magnitudes for each qubit. By assessing various working points throughout these scans, the analysis eliminates certain operation points by measuring if the frequency and amplitude lie within a tolerance of 250 MHz and 60 mV. If a candidate point does not lie within these tolerances, that point is eliminated.
To be suitable candidates for the CZ-gate, one qubit has to go to the ground state and the second one to the second excited state when a half-duration CZ-pulse is applied. A good estimation of the duration of the CZ-gate is 240 ns, so this means a 120 ns pulse is applied.
This is checked by initializing the two qubits to be in the excited state, and after the half duration CZ-pulse is applied, the two qubits are measured. The parameters that are swept for this measurement are the amplitude, from 0.1 V to 0.8 V, and the frequency detuning from -20 MHz to 20 MHz. When this is done, the maximum point is found for one qubit and the minimum point for the other qubit, see Figure 4.31. If these points are within a threshold, the CZ-current point is saved, but if the two points are outside the threshold, that current point is discarded. The measurement is done for all CZ-current candidates. For those candidates that pass, the amplitude and corrected frequency are saved for each passing candidate.

### 4.6.5 CZ calibration for working points

Each calibration sequence begins by preparing a pair of transmon qubits connected via a tunable coupler. The CZ pulse applied to the coupler is a soft square pulse with fixed duration (240 ns) and tunable amplitude and frequency provided as working point parameters.
At the start of each shot, all relevant qubits are reset. The control qubit is excited using an $X$ gate, and the target qubit is rotated by $X_{90}$ to initialize the Ramsey sequence. After a short buffer delay, the CZ pulse is applied to the coupler. This interaction induces a phase shift on the target qubit, conditional on the state of the control qubit. A second $X$ gate is then applied to the control qubit, and the Ramsey

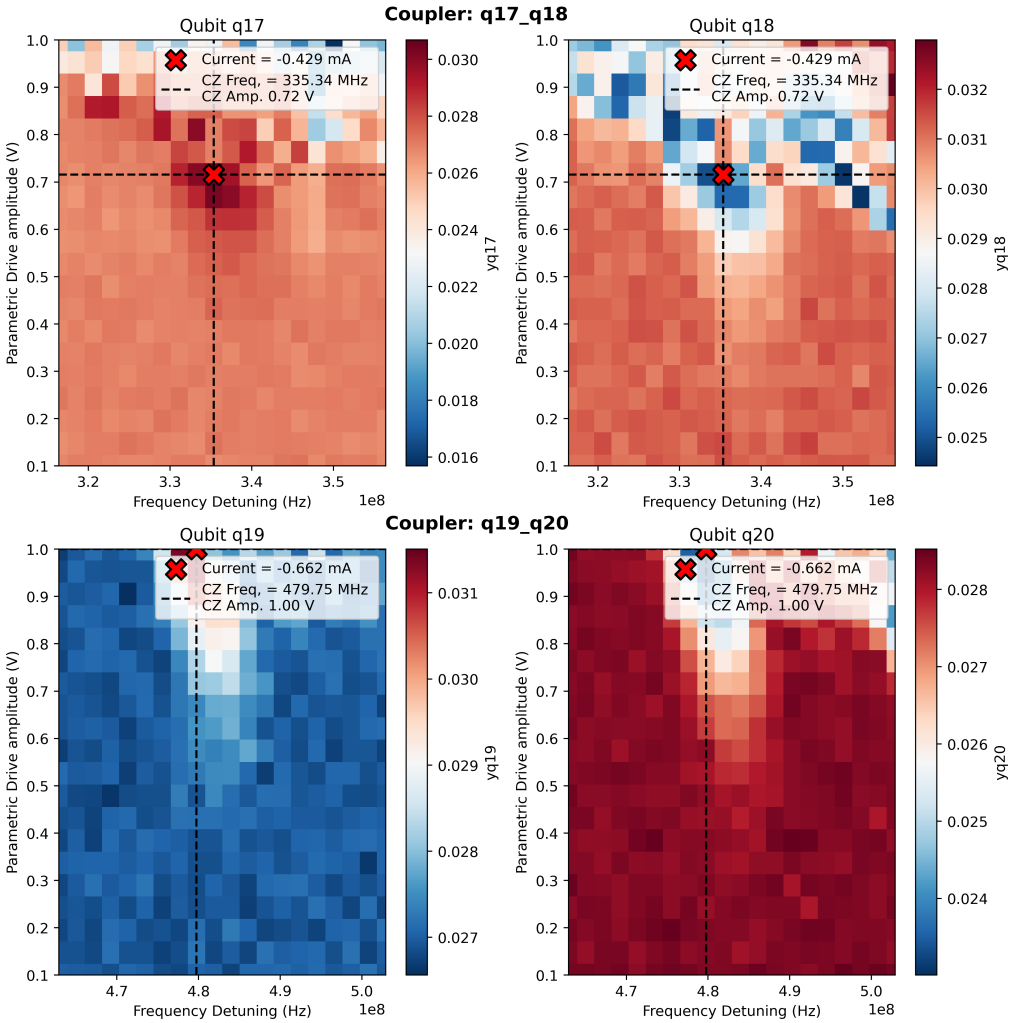


**Figure 4.31:** The plot shows CZ-parametrization for a passing candidate for two paris of coupled qubits. This means that qubit q17 and q19 will go to the excited state and qubit q18 and q20 will go to the ground state. The maxima and minima are located in the same cell, which makes them a good candidate. The flux points are not necessarily the best working points.

sequence is closed with a phase gate $R_{xy}(90, \phi)$ applied to the target qubit [13], illustrated in Figure 4.32.

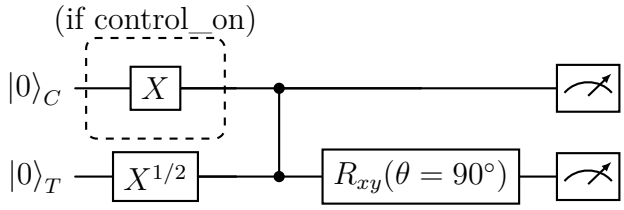


**Figure 4.32:** Circuit representation of the CZ calibration routine. The control qubit is optionally excited based on the `control_on` parameter. A CZ pulse is applied between the control and target qubits. The target qubit undergoes a Ramsey-style sequence with a final $R_{xy}$ rotation with a frequency sweep.

The final state of each qubit is measured using three-state single-shot readout. This is repeated over a range of Ramsey phases to extract the accumulated phase induced by the CZ gate. Each scan is supplemented with three calibration points corresponding to the preparation of the $|0\rangle$, $|1\rangle$, and $|2\rangle$ states, allowing accurate classification of measurement outcomes. This is done for all the remaining working points that have not been discarded by the CZ-parametrization measurement.

This static calibration procedure provides direct access to the phase acquired during the CZ operation. The figure of merit used to select the best working point among all candidates is the phase; the best working point is the one with the phase closest to $\pi$. This will be the optimal working point for the CZ-gate, see Figure 4.33.

Performing the measurements on all the remaining candidates, one candidate remains, which is the working point that will be most suitable for the CZ-gate. One also wants to make sure that the working point does not cause too much leakage. This can be seen in the control qubit. This measurement can also be done by swapping the target and control qubits. The working point should show a 180-degree phase shift even after a swap.

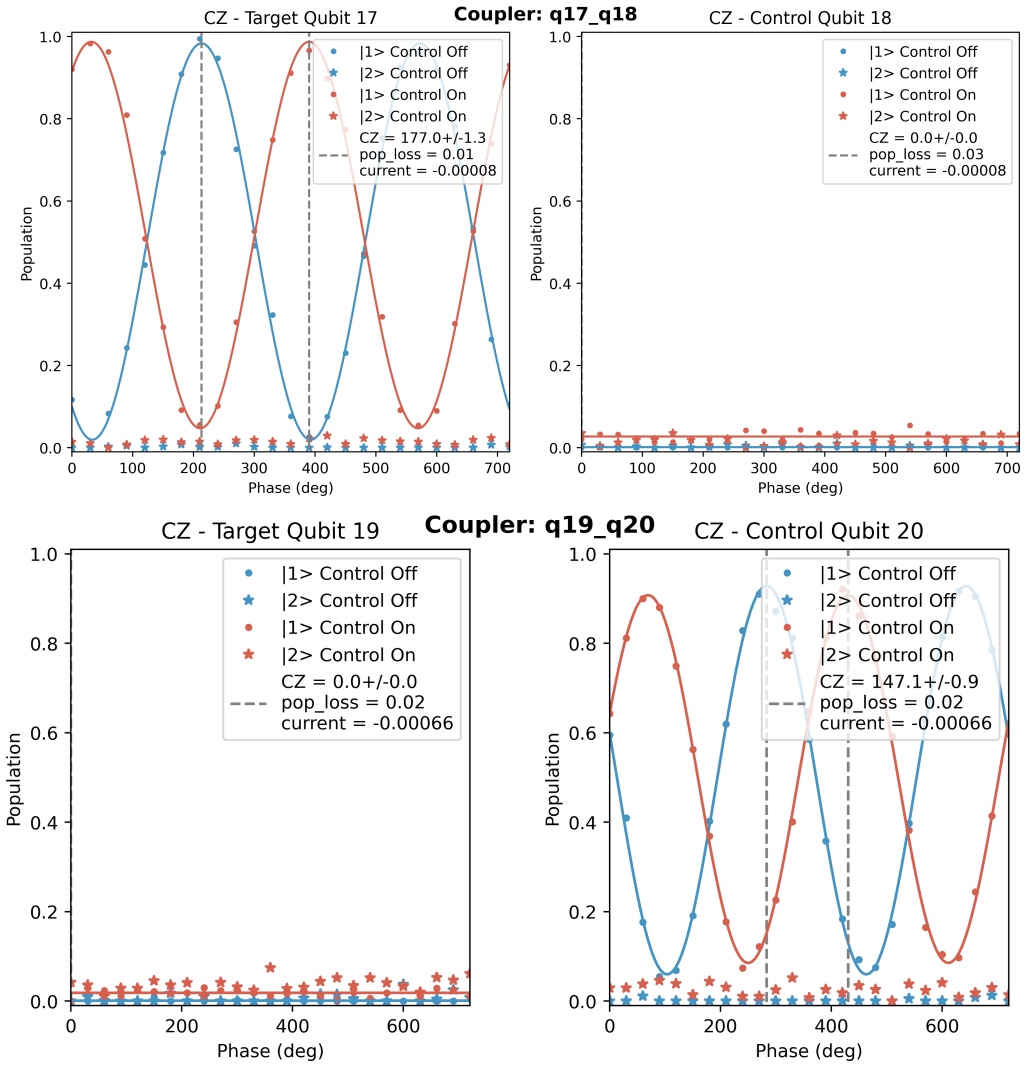


**Figure 4.33:** The figure shows the most suitable working point for the CZ-calibration, giving a 177-degree phase shift for qubit q17 and a 147-degree phase shift for qubit q20. Qubit q18 and q20 show the leakage; having a long stable value, as demonstrated in the figures is desirable.

### 4.6.6 Dynamic Phase Correction

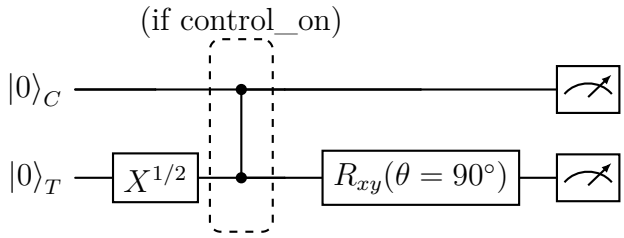


**Figure 4.34:** Circuit representation of the CZ dynamic phase routine. A CZ pulse is applied between the control and target qubits based on the `control_on` parameter. The target qubit undergoes a Ramsey-style sequence with a final $R_{xy}$ rotation with a frequency sweep.

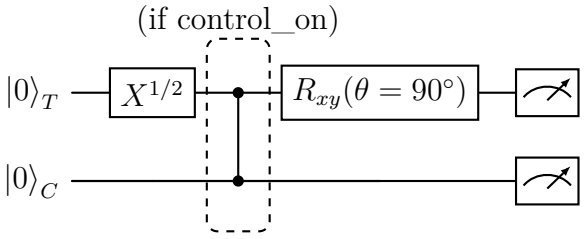


**Figure 4.35:** Circuit representation of the CZ dynamic phase routine. A CZ pulse is applied between the control and target qubits based on the `control_on` parameter. The target qubit undergoes a Ramsey-style sequence with a final $R_{xy}$ rotation with a frequency sweep.

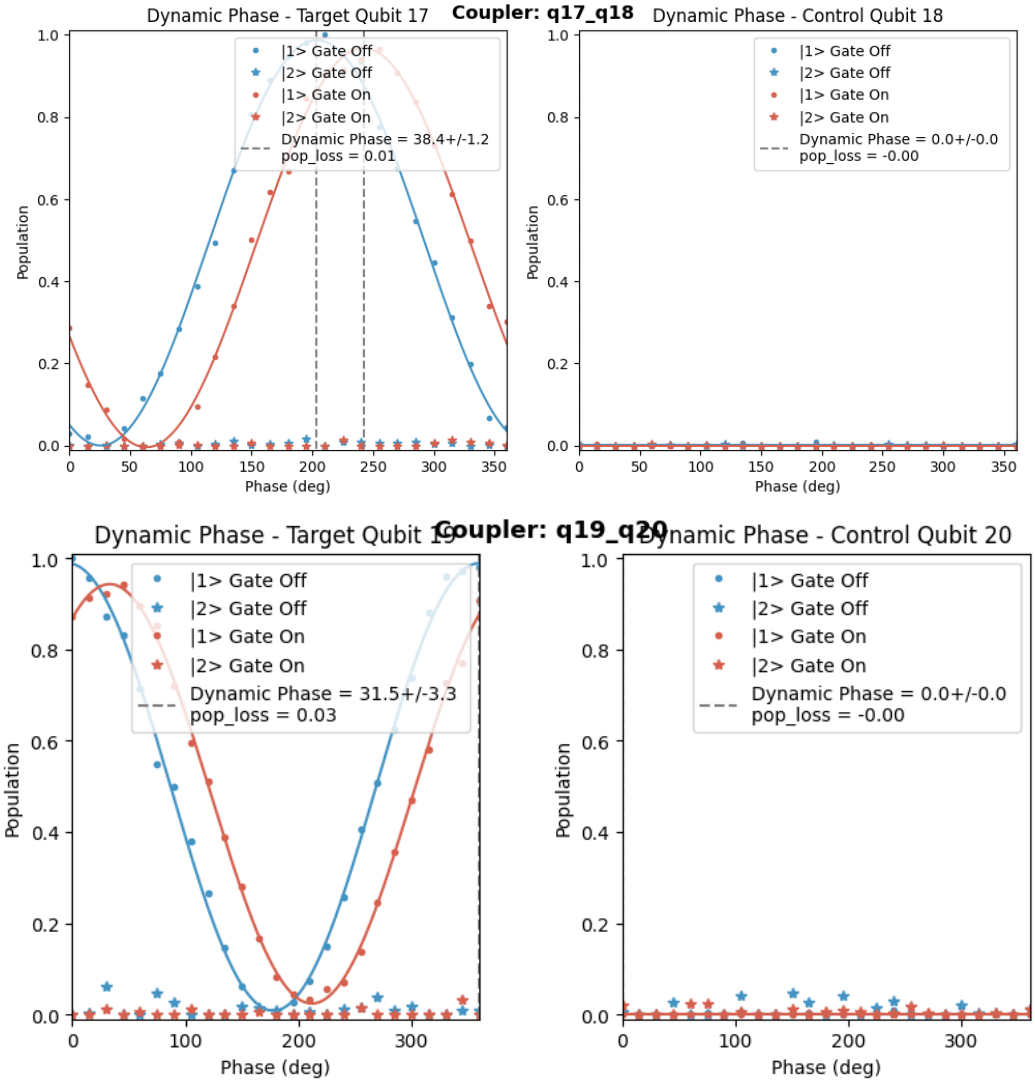


**Figure 4.36:** Measurement of the dynamic phase for qubit q17 is calculated to be 38.4 degrees and for qubit q19, 31.5 degrees.

Despite successfully inducing the CZ interaction, the flux modulation can introduce unwanted local phase shifts on individual qubits. These dynamic phases arise from temporary detuning and residual interactions during the gate. If uncorrected, they can accumulate and lead to logical errors across gate sequences [13]. To quantify and remove these shifts, Ramsey interferometry is used. The target qubit is placed in a superposition state, the CZ gate is applied, and the resulting interference pattern reveals any phase offset. The pulse scheme is illustrated in Figure 4.35. This is done for both qubits by swapping the target qubit and the control qubit. These offsets are then corrected using virtual $Z$ gates, which adjust the phase frame of each qubit without introducing additional physical operations. This step ensures that the implemented gate closely approximates an ideal CZ gate in the computational subspace.

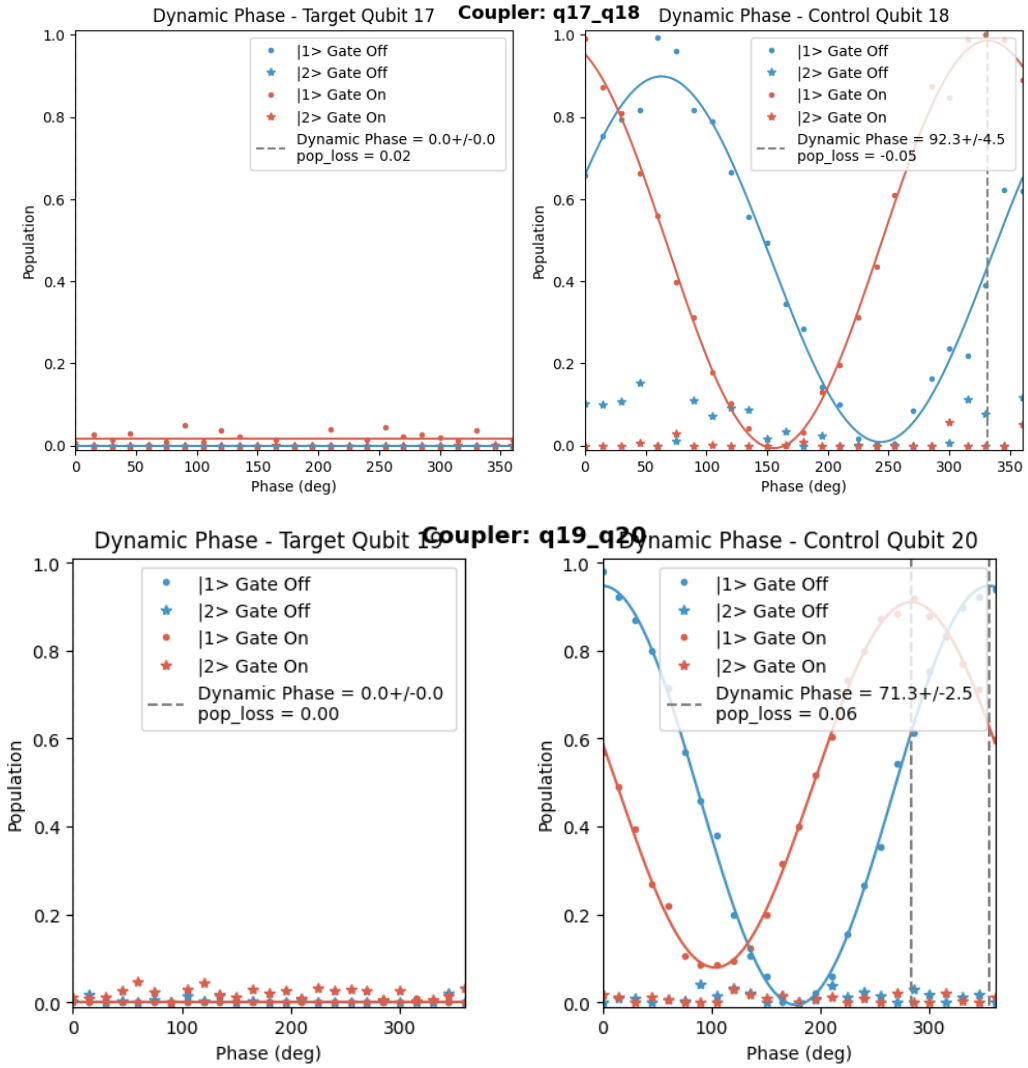


**Figure 4.37:** Measurement of the dynamic phase for qubit q18 is calculated to be 92.3 degrees and for qubit q20, 71.3 degrees.

Figures 4.36 and 4.37 show the shifts between the two fits are the dynamic phases for the qubits. To measure the dynamic phase for the other qubit, the target qubit and control qubit are swapped. Dynamic phases are used for two virtual Z-gates before performing the CZ-gate. This ensures that the only shift occurs when both qubits are in the excited state, by artificially applying a phase shift to correct for the unwanted dynamic phases in the CZ-gate.

## 4.7 Calibration time

The time required to run all the nodes in the calibrations is presented in Table 4.2. The total single-qubit time is around 10 minutes and is only needed to do once to calibrate the chip. The two-qubit calibration requires two and a half hours to calibrate a coupler group. This is estimated by comparing a single coupler and a multiple coupler calibration. Since 4 coupler groups need to be calibrated, a total

calibration time for the chip is estimated to be about 10 hours. It is important to stress that this is the time needed for the so-called bring-up calibration, i.e. the calibration that need to be run on a new chip or if significant changes occurred to the system, i.e. a temperature cycle. A faster calibration can be achieved for daily calibrations where only the CZ need to be recalibrated; this is estimated to take less than an hour. These are acceptable time scales for the two different calibration types.

| **Calibration** | **Time to run the node** |
|---|---|
| Resonator spectroscopy | 9 seconds |
| Qubit spectroscopy | 1 minute |
| Rabi oscillations | 31 seconds |
| Ramsey correction | 1 minute 33 seconds |
| Motzoi calibration | 1 minute 18 seconds |
| n-Rabi calibration | 1 minute 2 seconds |
| Readout frequency optimization | 3 minutes |
| Readout amplitude optimization | 30 seconds |
| **Total single qubit calibration** | 10 minutes |
| Qubit spectroscopy as a function of the flux* | 80 minutes |
| Resonator spectroscopy was a function of the flux* | 40 minutes |
| CZ current from spectroscopies* | 1 second |
| CZ parametrization with fixed duration* | $\approx 20$ minutes |
| CZ calibration | $\approx 10$ minutes |
| CZ dynamic phase | 1 minute |
| **Total for chip bring up** | $\approx 10$ hour |
| **Total for daily calibration** | $\approx 40$ minutes |

**Table 4.2:** This table summarizes all the calibration steps and how long each node takes. Steps marked with a * are not required for daily calibration.

# 5
# Conclusion and future directions

This chapter summarises the thesis. Ideas for future development will be suggested to achieve automatic two-qubit-gate calibration.

## 5.1 Conclusions

The series of experiments and selection developed in this work can be used to calibrate a CZ gate. The measurements can run in parallel, significantly speeding up the calibration process. To calibrate the whole chip for a total calibration time of 10h. Subsequent calibration will only need to re-calibrate the selected working point, hence can be done in less than 60 minutes.
Crucially, the process described in this thesis can be used to automatically select a bias point, something that was not done in either [12, 46], where the authors select without much motivation a flux point, or previous work in the group where a long manual scan was performed to find a suitable bias point. This means that after a temperature cycle, the chip can be calibrated in less than a day. Therefore, the Quantum Computing group will be able to speed up the development of new chips thanks to the faster evaluation time of each chip.
Unfortunately, it is difficult to quantify the performance of the procedure without measuring the fidelity of the gate using RB. Developing such a routine proved to be complex due to the required parallelization. Nevertheless, the small leakage measured in the calibration step and the phase difference close to 180 degrees are an indication that the performance should not be too poor.

## 5.2 Future directions

Several improvements could be made in the calibration process. Firstly, it is essential to run the two-qubit randomized benchmarking on the calibrated gates. This would provide a figure of merit for further analysis and is essential to both validate the work carried out and to evaluate any additional improvement. For example, the fidelity measured in randomized benchmarking could replace the 180-degree phase shift as the figure of merit for the working point candidate selection. This is a more reliable selection criteria and therefore should provide a better calibration.
In case of the fidelities being low, an idea to improve them would be to run the single-qubit calibration at the flux point of each candidate working point. This is relevant since the flux applied to the coupler causes the resonator/qubit frequencies to shift.

A measurement that is usually done when calibrating the CZ-gate is the CZ-chevron. This measurement could be used to optimize the gate time, but also further refine the frequency of the CZ. This procedure would have the potential to improve the fidelity of the CZ-gate. The drawback of including this procedure is the time it would add to the calibration procedure. Further RD is needed to evaluated both gains and time required by this additional step.

# Bibliography


[1] Quantum Zeitgeist. *Quantum Computing's Impact On Optimization Problems*. 2024. URL: https://quantumzeitgeist.com/quantum-computings-impact-on-optimization-problems/.

[2] V. Sehrawat. "Quantum Computing: Algorithms and Applications in Optimization Problems". In: *J. of Quantum Sci. Tech.* 1.2 (2024), pp. 18–22. DOI: 10.36676/jqst.v1.i2.11.

[3] Bela Bauer et al. "Quantum Algorithms for Quantum Chemistry and Quantum Materials Science". In: *Chemical Reviews* 120.22 (Oct. 2020), pp. 12685–12717. ISSN: 1520-6890. DOI: 10.1021/acs.chemrev.9b00829. URL: http://dx.doi.org/10.1021/acs.chemrev.9b00829.

[4] Daniel Koch et al. "Demonstrating NISQ era challenges in algorithm design on IBM's 20 qubit quantum computer". In: *AIP Advances* 10 (Sept. 2020), p. 095101. DOI: 10.1063/5.0015526.

[5] Davide Castelvecchi. *'A Truly Remarkable Breakthrough': Google's New Quantum Chip Achieves Accuracy Milestone*. Accessed: 2025-06-10. 2024. DOI: 10.1038/d41586-024-04028-3. URL: https://doi.org/10.1038/d41586-024-04028-3.

[6] USC Viterbi / Dornsife. *A new method for characterizing quantum gate errors*. "Quantum computing is ultimately limited by how accurately we can implement gates — the basic operations of a quantum processor." 2025. URL: https://today.usc.edu/a-new-method-for-characterizing-quantum-gate-errors.

[7] Eric Hyyppä et al. "Reducing Leakage of Single-Qubit Gates for Superconducting Quantum Processors Using Analytical Control Pulse Envelopes". In: *PRX Quantum* 5 (3 Sept. 2024), p. 030353. DOI: 10.1103/PRXQuantum.5.030353. URL: https://link.aps.org/doi/10.1103/PRXQuantum.5.030353.

[8] Yilun Xu et al. *Automatic Qubit Characterization and Gate Optimization with QubiC*. 2021. arXiv: 2104.10866 [quant-ph]. URL: https://arxiv.org/abs/2104.10866.

[9] Sandoko Kosen et al. "Signal Crosstalk in a Flip-Chip Quantum Processor". In: *PRX Quantum* 5.3 (Sept. 2024). ISSN: 2691-3399. DOI: 10.1103/prxquantum.5.030350. URL: http://dx.doi.org/10.1103/PRXQuantum.5.030350.

[10] Chalmers quantum computing group CNL. *Tergite Autocalibration*. https://github.com/tergite/autocalibration/tree/v2024.09.0. 2025.

[11] Michael A. Nielsen and Isaac L. Chuang. *Quantum Computation and Quantum Information: 10th Anniversary Edition*. Cambridge University Press, 2010.

[12] M. Ganzhorn et al. “Benchmarking the noise sensitivity of different parametric two-qubit gates in a single superconducting quantum computing platform”. In: *Phys. Rev. Res.* 2 (3 Sept. 2020), p. 033447. DOI: 10.1103/PhysRevResearch.2.033447. URL: https://link.aps.org/doi/10.1103/PhysRevResearch.2.033447.

[13] M. Ganzhorn et al. “Benchmarking the noise sensitivity of different parametric two-qubit gates in a single superconducting quantum computing platform”. In: *Physical Review Research* 2.3 (Sept. 2020). ISSN: 2643-1564. DOI: 10.1103/physrevresearch.2.033447. URL: http://dx.doi.org/10.1103/PhysRevResearch.2.033447.

[14] B.D. Josephson. “Possible new effects in superconductive tunnelling”. In: *Physics Letters* 1.7 (1962), pp. 251–253. ISSN: 0031-9163. DOI: https://doi.org/10.1016/0031-9163(62)91369-0. URL: https://www.sciencedirect.com/science/article/pii/0031916362913690.

[15] Lutz Finger. “The Josephson junction circuit family: Network theory”. In: *International Journal of Circuit Theory and Applications - INT J CIRCUIT THEOR APPL* 28 (July 2000), pp. 371–420. DOI: 10.1002/1097-007X(200007/08)28:43.0.CO;2-O.

[16] Sergio Boixo et al. “Characterizing quantum supremacy in near-term devices”. In: *Nature Physics* 14.6 (Apr. 2018), pp. 595–600. ISSN: 1745-2481. DOI: 10.1038/s41567-018-0124-x. URL: http://dx.doi.org/10.1038/s41567-018-0124-x.

[17] Jens Koch et al. “Charge-insensitive qubit design derived from the Cooper pair box”. In: *Physical Review A* 76.4 (Oct. 2007). ISSN: 1094-1622. DOI: 10.1103/physreva.76.042319. URL: http://dx.doi.org/10.1103/PhysRevA.76.042319.

[18] B. G. Christensen et al. “Anomalous charge noise in superconducting qubits”. In: *Physical Review B* 100.14 (Oct. 2019). ISSN: 2469-9969. DOI: 10.1103/physrevb.100.140503. URL: http://dx.doi.org/10.1103/PhysRevB.100.140503.

[19] Zihao Wang et al. “High-$E_J/E_C$ transmon qudits with up to 12 levels”. In: *Phys. Rev. Appl.* 23 (3 Mar. 2025), p. 034046. DOI: 10.1103/PhysRevApplied.23.034046. URL: https://link.aps.org/doi/10.1103/PhysRevApplied.23.034046.

[20] Johannes M. Fink. “Quantum Nonlinearities in Strong Coupling Circuit Qed”. In: 2011. URL: https://api.semanticscholar.org/CorpusID:125104238.

[21] Philip Krantz. *Investigation of Transmon Qubit Designs - A Study of Plasma Frequency Predictability*. 2010. URL: https://odr.chalmers.se/items/d909ca85-d5d2-4b81-948f-fb7577f2da2d.

[22] Thomas E. Roth, Ruichao Ma, and Weng C. Chew. “The Transmon Qubit for Electromagnetics Engineers: An introduction”. In: *IEEE Antennas and Propagation Magazine* 65.2 (Apr. 2023), pp. 8–20. ISSN: 1558-4143. DOI: 10.1109/map.2022.3176593. URL: http://dx.doi.org/10.1109/MAP.2022.3176593.

[23] L.B. Gordon et al. “Electrical insulation at cryogenic temperatures”. In: *Proceedings of Conference on Electrical Insulation and Dielectric Phenomena - CEIDP ’96*. Vol. 1. 1996, 56 vol.1-. DOI: 10.1109/CEIDP.1996.564588.

[24] Fei Yan et al. “Tunable Coupling Scheme for Implementing High-Fidelity Two-Qubit Gates”. In: *Physical Review Applied* 10.5 (Nov. 2018). ISSN: 2331-7019. DOI: 10.1103/physrevapplied.10.054062. URL: http://dx.doi.org/10.1103/PhysRevApplied.10.054062.

[25] David C. McKay et al. “Universal Gate for Fixed-Frequency Qubits via a Tunable Bus”. In: *Physical Review Applied* 6.6 (Dec. 2016). ISSN: 2331-7019. DOI: 10.1103/physrevapplied.6.064007. URL: http://dx.doi.org/10.1103/PhysRevApplied.6.064007.

[26] Daniel Malz and Adam Smith. “Topological Two-Dimensional Floquet Lattice on a Single Superconducting Qubit”. In: *Physical Review Letters* 126.16 (Apr. 2021). ISSN: 1079-7114. DOI: 10.1103/physrevlett.126.163602. URL: http://dx.doi.org/10.1103/PhysRevLett.126.163602.

[27] Amr Osman et al. “Mitigation of frequency collisions in superconducting quantum processors”. In: *Phys. Rev. Res.* 5 (4 Oct. 2023), p. 043001. DOI: 10.1103/PhysRevResearch.5.043001. URL: https://link.aps.org/doi/10.1103/PhysRevResearch.5.043001.

[28] Qblox. *Product Overview*. Accessed: 2025-06-09. Qblox. 2025. URL: https://docs.qblox.com/en/main/getting_started/product_overview.html.

[29] Qblox. *SPI Rack*. Accessed: 2025-06-09. Qblox. 2025. URL: https://docs.qblox.com/en/main/tutorials/SPI/spi_rack.html.

[30] Quantify. *About Quantify-scheduler*. Accessed: 2025-06-09. Quantify. 2025. URL: https://quantify-os.org/docs/quantify-scheduler/v0.20.1/user/about.html.

[31] François Mallet et al. “Single-shot qubit readout in circuit quantum electrodynamics”. In: *Nature Physics* 5.11 (Sept. 2009), pp. 791–795. ISSN: 1745-2481. DOI: 10.1038/nphys1400. URL: http://dx.doi.org/10.1038/nphys1400.

[32] John P. T. Stenger et al. “Simulating spectroscopy experiments with a superconducting quantum computer”. In: *Phys. Rev. Res.* 4 (4 Nov. 2022), p. 043106. DOI: 10.1103/PhysRevResearch.4.043106. URL: https://link.aps.org/doi/10.1103/PhysRevResearch.4.043106.

[33] Zijun Chen. “Metrology of Quantum Control and Measurement in Superconducting Qubits”. In: 2018. URL: https://api.semanticscholar.org/CorpusID:196194358.

[34] I. I. Rabi. “Space Quantization in a Gyrating Magnetic Field”. In: *Phys. Rev.* 51 (8 Apr. 1937), pp. 652–654. DOI: 10.1103/PhysRev.51.652. URL: https://link.aps.org/doi/10.1103/PhysRev.51.652.

[35] S.E. Rasmussen et al. “Superconducting Circuit Companion—an Introduction with Worked Examples”. In: *PRX Quantum* 2 (4 Dec. 2021), p. 040204. DOI: 10.1103/PRXQuantum.2.040204. URL: https://link.aps.org/doi/10.1103/PRXQuantum.2.040204.

[36] F. Motzoi et al. “Simple Pulses for Elimination of Leakage in Weakly Nonlinear Qubits”. In: *Physical Review Letters* 103.11 (Sept. 2009). ISSN: 1079-7114. DOI:

10.1103/physrevlett.103.110501. URL: http://dx.doi.org/10.1103/PhysRevLett.103.110501.

[37] J. M. Gambetta et al. "Analytic control methods for high-fidelity unitary operations in a weakly nonlinear oscillator". In: *Physical Review A* 83.1 (Jan. 2011). ISSN: 1094-1622. DOI: 10.1103/physreva.83.012308. URL: http://dx.doi.org/10.1103/PhysRevA.83.012308.

[38] Liangyu Chen et al. "Transmon qubit readout fidelity at the threshold for quantum error correction without a quantum-limited amplifier". In: *npj Quantum Information* 9.1 (Mar. 2023). ISSN: 2056-6387. DOI: 10.1038/s41534-023-00689-6. URL: http://dx.doi.org/10.1038/s41534-023-00689-6.

[39] Joseph Emerson, Robert Alicki, and Karol Życzkowski. "Scalable noise estimation with random unitary operators". In: *Journal of Optics B: Quantum and Semiclassical Optics* 7.10 (Sept. 2005), S347–S352. ISSN: 1741-3575. DOI: 10.1088/1464-4266/7/10/021. URL: http://dx.doi.org/10.1088/1464-4266/7/10/021.

[40] Daniel Gottesman. "Theory of fault-tolerant quantum computation". In: *Physical Review A* 57.1 (Jan. 1998), pp. 127–137. ISSN: 1094-1622. DOI: 10.1103/physreva.57.127. URL: http://dx.doi.org/10.1103/PhysRevA.57.127.

[41] Robin Blume-Kohout, Kenneth Rudinger, and Timothy Proctor. *Easy better quantum process tomography*. 2025. arXiv: 2412.16293 [quant-ph]. URL: https://arxiv.org/abs/2412.16293.

[42] E. Knill et al. "Randomized benchmarking of quantum gates". In: *Physical Review A* 77.1 (Jan. 2008). ISSN: 1094-1622. DOI: 10.1103/physreva.77.012307. URL: http://dx.doi.org/10.1103/PhysRevA.77.012307.

[43] Yangsen Ye et al. "Realization of High-Fidelity Controlled-Phase Gates in Extensible Superconducting Qubits Design with a Tunable Coupler". In: *Chinese Physics Letters* 38.10 (Nov. 2021), p. 100301. ISSN: 1741-3540. DOI: 10.1088/0256-307x/38/10/100301. URL: http://dx.doi.org/10.1088/0256-307X/38/10/100301.

[44] Cora N. Barrett et al. "Learning-Based Calibration of Flux Crosstalk in Transmon Qubit Arrays". In: *Physical Review Applied* 20.2 (Aug. 2023). ISSN: 2331-7019. DOI: 10.1103/physrevapplied.20.024070. URL: http://dx.doi.org/10.1103/PhysRevApplied.20.024070.

[45] P. Krantz et al. "A quantum engineer's guide to superconducting qubits". In: *Applied Physics Reviews* 6.2 (June 2019). ISSN: 1931-9401. DOI: 10.1063/1.5089550. URL: http://dx.doi.org/10.1063/1.5089550.

[46] Rui Li et al. "Realization of High-Fidelity CZ Gate Based on a Double-Transmon Coupler". In: *Physical Review X* 14.4 (Nov. 2024). ISSN: 2160-3308. DOI: 10.1103/physrevx.14.041050. URL: http://dx.doi.org/10.1103/PhysRevX.14.041050.

[47] Taryn V. Stefanski et al. *Improved fluxonium readout through dynamic flux pulsing*. 2024. arXiv: 2411.13437 [quant-ph]. URL: https://arxiv.org/abs/2411.13437.

**Department Of Microtechnology And Nanoscience**
**CHALMERS UNIVERSITY OF TECHNOLOGY**
Gothenburg, Sweden
www.chalmers.se


CHALMERS
UNIVERSITY OF TECHNOLOGY